

Search for decay $\Upsilon(5S) \rightarrow \gamma W_{bj}$

Nicholas Corrado, Vladimir Savinov

University of Pittsburgh, Pittsburgh, PA-15260, USA

Abstract

The recent discovery of the states Z_b and Z'_b implies the possible existence of a new family of hadronic resonances including molecular states dubbed W_{bJ} . We describe a search for W_{bJ} in the decay $\Upsilon(5S) \rightarrow \gamma W_{bJ}$ using 121.4 fb^{-1} of data collected at the $\Upsilon(5S)$ resonance with the Belle detector at the KEKB asymmetric-energy electron-positron collider. Using Monte Carlo simulation, we study Belle's sensitivity to the decay $\Upsilon(5S) \rightarrow \gamma W_{bJ}$, search for its presence in Belle data and describe the procedure we would use to establish an upper limit on the visible production cross section for these new states.

16 Contents

17	1 Introduction	1
18	1.1 Motivation	1
19	1.2 New Spectroscopy	1
20	1.3 Radiative Decays $\Upsilon(5S) \rightarrow \gamma W_{bJ}$	2
21	1.4 Expected Signal in Data	4
22	2 Monte Carlo and Data Samples	5
23	3 Selection Criteria	6
24	3.1 Selection of Photon Candidates	6
25	3.2 Selection of Pion and Muon Candidates	6
26	3.3 Selection of $\Upsilon(5S)$ Candidates	7
27	3.4 Best Candidate Selection	7
28	4 Signal Monte Carlo Studies	8
29	4.1 Signal Monte Carlo Distributions	8
30	4.2 Description of the Signal Region	9
31	4.3 Trigger Simulation	12
32	5 Background Studies	12
33	5.1 Generic Monte Carlo and Blinded Data	12
34	6 Background from $\Upsilon(5S) \rightarrow \Upsilon(1S)\pi^+\pi^-$ with Initial State Radiation (ISR)	15
35	6.1 $\Upsilon(5S) \rightarrow \Upsilon(1S)\pi^+\pi^-$ ISR Monte Carlo Sample	17
36	6.2 Background Shape of $\Upsilon(5S) \rightarrow \Upsilon(1S)\pi^+\pi^-$ with ISR	18
37	7 Contribution from $\Upsilon(5S) \rightarrow Z_b^{(\prime)\pm}\pi^\mp$	20
38	8 Fitting	24
39	8.1 Signal and Background PDFs	24
40	8.2 Confidence Belts	25
41	8.3 Linearity Study	25
42	8.4 Sensitivity Estimation	26
43	9 Summary	29
44	10 Appendix	30
45	10.1 Final State Radiation	30

46 List of Figures

47	1	Pure $b\bar{b}$ bottomonium mass spectrum for a relativized quark model	2
48	2	Spectrum of bottomonium and bottomonium-like mesons.	3
49	3	Expected family of molecular isotriplet resonances.	5
50	4	Signal MC distributions	8
51	5	$M(\pi^+\pi^+\mu^+\mu^-)$ and $M(\pi^+\pi^-(\mu^+\mu^-)_{\text{fit}})$ resolutions for signal events	10
52	6	ΔE resolution and quantities contributing to ΔE resolution.	11
53	7	Definitions of important regions	13
54	8	Offline trigger selection for reconstructed signal MC events.	14
55	9	Offline trigger efficiency for reconstructed signal MC events.	15
56	10	Identifying background present in data but not in generic MC.	16
57	11	Motivation for ISR studies.	17
58	12	Reweighted ISR energy spectrum	18
59	13	Background due to ISR.	19
60	14	Effect of decay models on $M(\pi^+\pi^-(\mu^+\mu^-)_{\text{fit}})$ distribution.	20
61	15	Effect of decay models on muon angular distribution.	21
62	16	Effect of ΔE cut on ISR background shape.	22
63	17	Definitions of subdivisions of the grand sideband region	22
64	18	Distribution of $M(\pi^+\pi^-(\mu^+\mu^-)_{\text{fit}})$ vs $M_{\text{rec}}(\gamma)$ for $\Upsilon(5S) \rightarrow Z_b^{(\prime)\pm}\pi^\mp$ MC	23
65	19	Distribution of $M(\pi^+\pi^-(\mu^+\mu^-)_{\text{fit}})$ for $\Upsilon(5S) \rightarrow Z_b^{(\prime)\pm}\pi^\mp$	24
66	20	Fitting background MC and data	26
67	21	90% confidence belts for frequentist method.	27
68	22	Average $N_{\text{sig}}^{\text{fit}}$ for varying values of $N_{\text{sig}}^{\text{gen}}$	28
69	23	$N_{\text{sig}}^{\text{fit}}$ Distributions for ensemble tests with different $N_{\text{sig}}^{\text{gen}}$	29
70	24	Final state radiation from charged tracks	31

71 **List of Tables**

72	1	Possible molecular isotriplet states in decays of $\Upsilon(5S)$ and $\Upsilon(6S)$	4
73	2	EvtGen decay models used in Monte Carlo simulation of signal processes. . .	6
74	3	Selection criteria for $\Upsilon(5S) \rightarrow \gamma W_{bJ}$	7
75	4	Quantities contributing to widths of measured quantities	8
76	5	Definitions of the signal region and other important regions.	10
77	6	Backgrounds labeled in Fig. 10.	16
78	7	Decay models used in background ISR MC	19
79	8	Definitions of subdivisions of the grand sideband region	21
80	9	Comparing the number of events in ISR MC and blinded data in the subdivided grand sideband Region	23
81			
82	10	Values of fixed quantities in the signal PDF model	25
83	11	Values of quantities used in upper limit calculation	30

1 Introduction

1.1 Motivation

In this document, we describe a search for new hadronic states of matter – bottomonium-like particles dubbed W_{bJ} – in radiative decays of $\Upsilon(5S)$. These states are believed to be of molecular nature, where a pair of colored $B_{(s)}^{(*)}$ mesons, each containing a b or an anti- b quark, are held together by the strong interaction (in a way similar to single-pion exchange force mechanism in QCD-inspired low-energy models). As with conventional bottomonium, *i.e.* $b\bar{b}$ states, these molecular states exhibit their own spectroscopy. However, their masses and properties obviously could not be predicted using $q\bar{q}$ potential models. We are motivated by Belle’s discoveries [1, 2, 3, 4] of the $Z_b(10610)$ and $Z_b(10650)$ states (referred to in the rest of this document as Z_b and Z'_b or just Z_b) and theoretical predictions which use the molecular picture to explain the nature of the Z_b and predict the existence of additional hadronic states. These predictions can be used to explain various long-standing puzzles in the (no longer pure) bottomonium at energies above the threshold for B meson pair production.

1.2 New Spectroscopy

Since the discovery of the Υ meson, the b quark, and B mesons [5], conventional bottomonium states have been a rich source of information about strong interaction dynamics in the approximately non-relativistic $b\bar{b}$ system. Vector bottomonium and bottomonium-like states ($\Upsilon(nS)$ mesons) can be produced directly in the e^+e^- annihilation. Three of these states – $\Upsilon(1S)$, $\Upsilon(2S)$, and $\Upsilon(3S)$ – have masses below the $B\bar{B}$ threshold [6]. These states are believed to be pure $b\bar{b}$, and their properties are relatively easy to understand using potential models. Such relativized models [7] predict 34 $b\bar{b}$ bound states below $\Upsilon(4S)$ energy, 15 of which have been observed. We show the predictions for the energy levels in the $b\bar{b}$ spectroscopy [8, 9] in Fig. 1.

Hadronic transitions (such as, *e.g.* $\Upsilon(3S) \rightarrow \pi^+\pi^-\Upsilon(1S)$) between bottomonium states provide an excellent opportunity to study QCD dynamics in non-perturbative regime by comparing the measured masses, widths, branching fractions, angular and invariant mass distributions with the theoretical predictions. For pure bottomonium states – $b\bar{b}$ resonances below $B\bar{B}$ threshold – the hadronic transitions proceed via radiating the strong field, *i.e.*, by emitting the gluons which convert into light hadrons. States above $B\bar{B}$ threshold, starting with $\Upsilon(4S)$, are significantly wider than the lower-mass states, and their hadronic transitions are known to exhibit certain properties that are unexpected for pure $b\bar{b}$ states. While the latter are well described from the perspective of Heavy Quark Spin Symmetry (HQSS) where transitions involving the spin of the heavy b quark are strongly suppressed, the former states, including the $\Upsilon(5S)$, require a different explanation [10].

The favored explanation for the properties of $\Upsilon(5S)$, including its decays to Z_b , is based on the molecular picture, where these vector bottomonium-like resonances are assumed to contain an admixture of pairs of colored heavy mesons. This hypothesis has been successfully employed [11] to explain the decays to and the existence of the six Z_b states. However, the details of the interaction responsible for these processes are not yet fully understood. Alternative explanations include a model with a diquark-antidiquark pair, where a pair of

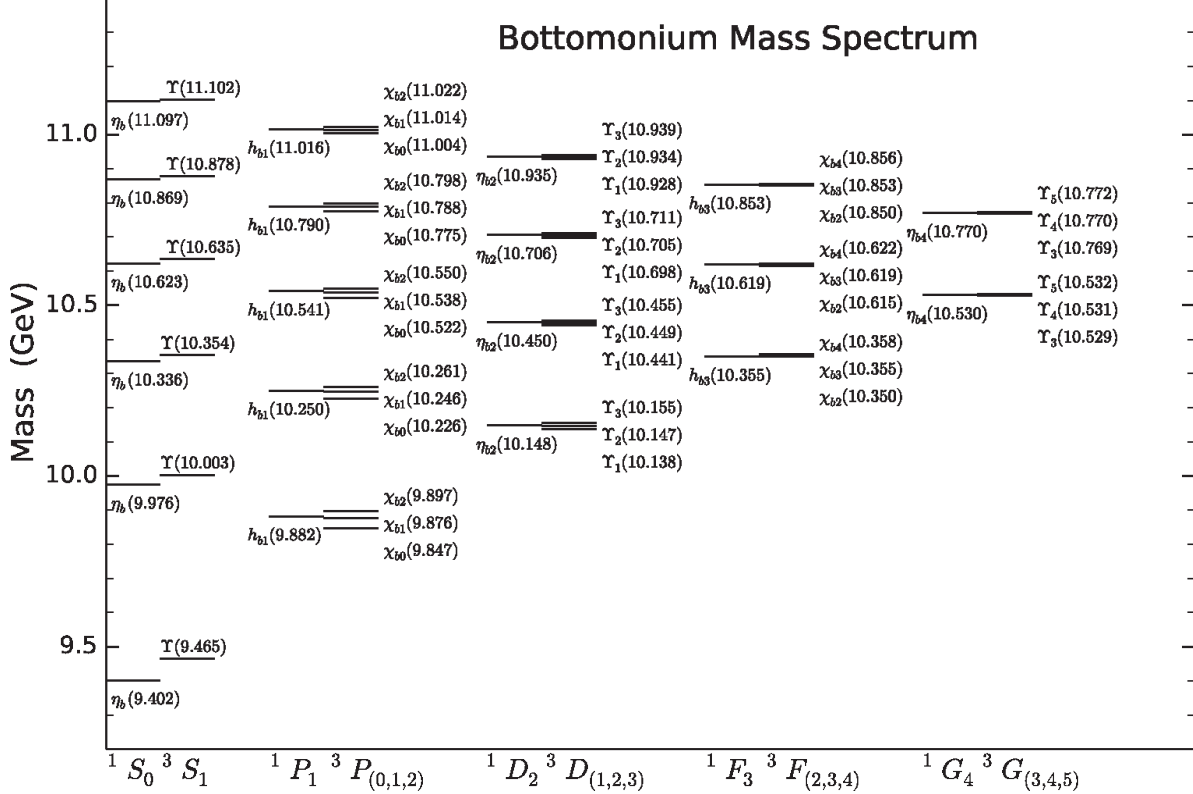


Figure 1: Pure (*i.e.* $b\bar{b}$) bottomonium mass spectrum [8] calculated using a relativized quark model [7].

125 quarks and a pair of antiquarks are each bound with a stronger force than the force holding
 126 diquark and antiquark together. While the search described in this document is model-
 127 independent, our motivation is somewhat biased in favor of the molecular picture and has
 128 likely impacted our decisions about how to perform the analysis.

129 The main goal of our study is to test some of the predictions of the new spectroscopy [12]
 130 that predicts energy levels for the molecular bottomonium-like states depicted in Fig. 2,
 131 Namely, we describe a search for the partner states of Z_b , referred to as W_{bJ} , and we aim to
 132 obtain new information about hadronic dynamics in presence of the heavy b quarks. Improv-
 133 ing the current understanding of such dynamics is of paramount importance for being able to
 134 use the hadronic decays of B mesons to extract possible contributions from the Beyond-the-
 135 Standard-Model (BSM) amplitudes, where the interplay between the strong interaction and
 136 the new BSM weak phases could not be reliably understood without the precise theoretical
 137 predictions for the QCD part.

138 1.3 Radiative Decays $\Upsilon(5S) \rightarrow \gamma W_{bJ}$

139 The Z_b states were discovered in single-pion transitions of $\Upsilon(5S)$ and $\Upsilon(6S)$, followed by
 140 another single-pion transition to the bottomonium states. According to molecular interpre-
 141 tation, $Z_b(10610)$ is primarily a $B\bar{B}^*$ state, while $Z_b(10650)$ (a.k.a. Z'_b) is a $B^*\bar{B}^*$ state.
 142 Z_b are spin-1 isotriplets (both neutral and charged states were discovered in transitions

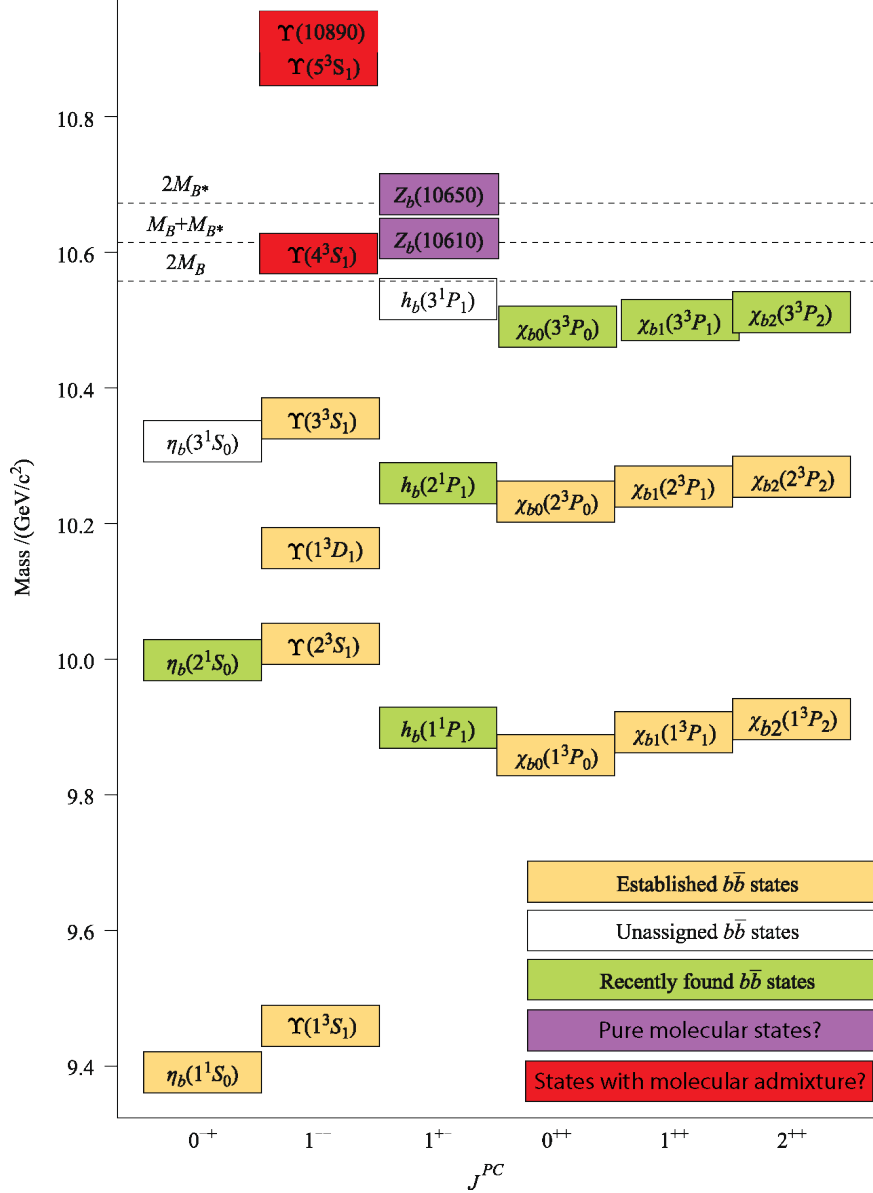


Figure 2: Most relevant (for our study) states in conventional bottomonium and bottomonium-like spectroscopies. We modified this figure from S. Olsen’s review article [12]. Note that we took liberty to modify the original figure to better represent the contents of this Note, namely, we relabeled $\Upsilon(nS)$ ($n = 4, 5, 6$) as “States with molecular admixture?” and Z_b states as “Pure molecular states?”.

143 $\Upsilon(nS) \rightarrow \pi Z_b$ ($n = 5, 6$). The hypothetical partners of positive G -parity states Z_b , *i.e.* the
144 W_{bJ} states, would also be isotriplets but of negative G -parity (quantum numbers of the new
145 molecular states are defined by quantum numbers of their partners in two-body decays of the
146 $\Upsilon(5S)$ parent: while Z_b is accompanied by a pion, each W_{bj} is accompanied by a ρ meson (or
147 a photon)). Therefore the W_{bJ} states are expected to appear in transitions $\Upsilon(nS) \rightarrow \rho W_{bJ}$.
148 Conservation of angular momentum allows J in W_{bJ} to be 0, 1 or 2. Excited states such as
149 W'_{b0} could exist as well. Quantum numbers assigned to Z_b and W_{bJ} states are summarized

$I^G(J^P)$	Name	Co-produced with (threshold, GeV/c ²)	Assumed composition	Decay channels
1 ⁺ (1 ⁺)	$Z_b(10610)$	π (10.75)	$B\bar{B}^*$	$\Upsilon(nS)\pi, h_b(nP)\pi, \eta_b(nS)\rho$
1 ⁺ (1 ⁺)	$Z'_b(10650)$	π (10.79)	$B^*\bar{B}^*$	$\Upsilon(nS)\pi, h_b(nP)\pi, \eta_b(nS)\rho$
1 ⁻ (0 ⁺)	W_{b0}	ρ (11.34), γ (10.56)	$B\bar{B}$	$\Upsilon(nS)\rho, \eta_b(nS)\pi, \chi_{b\pi}$
1 ⁻ (0 ⁺)	W'_{b0}	ρ (11.43), γ (10.65)	$B^*\bar{B}^*$	$\Upsilon(nS)\rho, \eta_b(nS)\pi, \chi_{b\pi}$
1 ⁻ (1 ⁺)	W_{b1}	ρ (11.38), γ (10.61)	$B\bar{B}^*$	$\Upsilon(nS)\rho, \chi_{b\pi}$
1 ⁻ (2 ⁺)	W_{b2}	ρ (11.43), γ (10.65)	$B^*\bar{B}^*$	$\Upsilon(nS)\rho, \chi_{b\pi}$

Table 1: Molecular isotriplet states which could be produced in the decays of $\Upsilon(5S)$ and $\Upsilon(6S)$ according to [10]. Note that the ρ could be replaced by a photon in the decays of $I_3 = 0$ states, but this would suppress the expected rate even more. Please see Fig. 3 as well.

150 in Table 1.

151 The $\Upsilon(5S)$ resonance does not have enough energy to allow the transition to W_{bJ} with
152 sufficient amount of energy left for the two pions in the tail of the ρ invariant mass. In
153 our analysis, instead of searching for decays with the ρ mesons, we have to allow for the $q\bar{q}$
154 annihilation and pay the price of approximately α_{em} in the branching fraction:

$$\frac{\Gamma(\Upsilon(5S) \rightarrow \gamma W_{bJ})}{\Gamma(\Upsilon(5S) \rightarrow Z_b\pi)} \sim \alpha_{\text{em}} \approx \frac{1}{137} \quad (1)$$

155 Therefore, we search for the transitions $\Upsilon(5S) \rightarrow \gamma W_{bJ}$. This indirect phase space limitation
156 allows us to search only for the $I_3 = 0$ partners of the Z_b states, *i.e.* only the neutral
157 component of each isotriplet can be found in such radiative transitions. We explain this
158 strategy, suggested [13] by M.B. Voloshin, in Fig. 3.

159 To search for all new resonances expected in the new spectroscopy would require to
160 collect a sizeable data sample at $\Upsilon(6S)$ or above its energy. Such possible future studies [14]
161 at Belle II and many more interesting discussions (such as possible existence of isoscalar
162 partners of Z_b and W_{bJ}) can be found elsewhere [10]. In the rest of this paper, we focus on
163 the analysis of the full $\Upsilon(5S)$ data sample where we search for the decay $\Upsilon(5S) \rightarrow \gamma W_{bJ}$.

164 1.4 Expected Signal in Data

165 Belle previously reported [15] that charged Z_b states comprise approximately 2.54% of the
166 1819 $\Upsilon(1S)\pi^+\pi^-$ (followed by $\Upsilon(1S) \rightarrow \mu^+\mu^-$) events observed with the full data sample.
167 The overall reconstruction efficiency in Z_b analysis was estimated to be around 46%. This
168 allows us to estimate that, with an ideal, *i.e.* 100% efficient detector, we would expect to
169 detect, approximately, 100 (charged) Z_b events.

170 While searching for W_{bJ} events in radiative decays of $\Upsilon(5S)$, as elaborated in Section 1.3,
171 we have to pay the price of α_{em} . Jumping a little bit ahead of ourselves, with our overall
172 detection efficiency of 29%, we therefore expect to observe, on average, 0.2 W_{b0} events. This
173 number, however, has a (hopefully very) large uncertainty, and, after all, we are (always!)

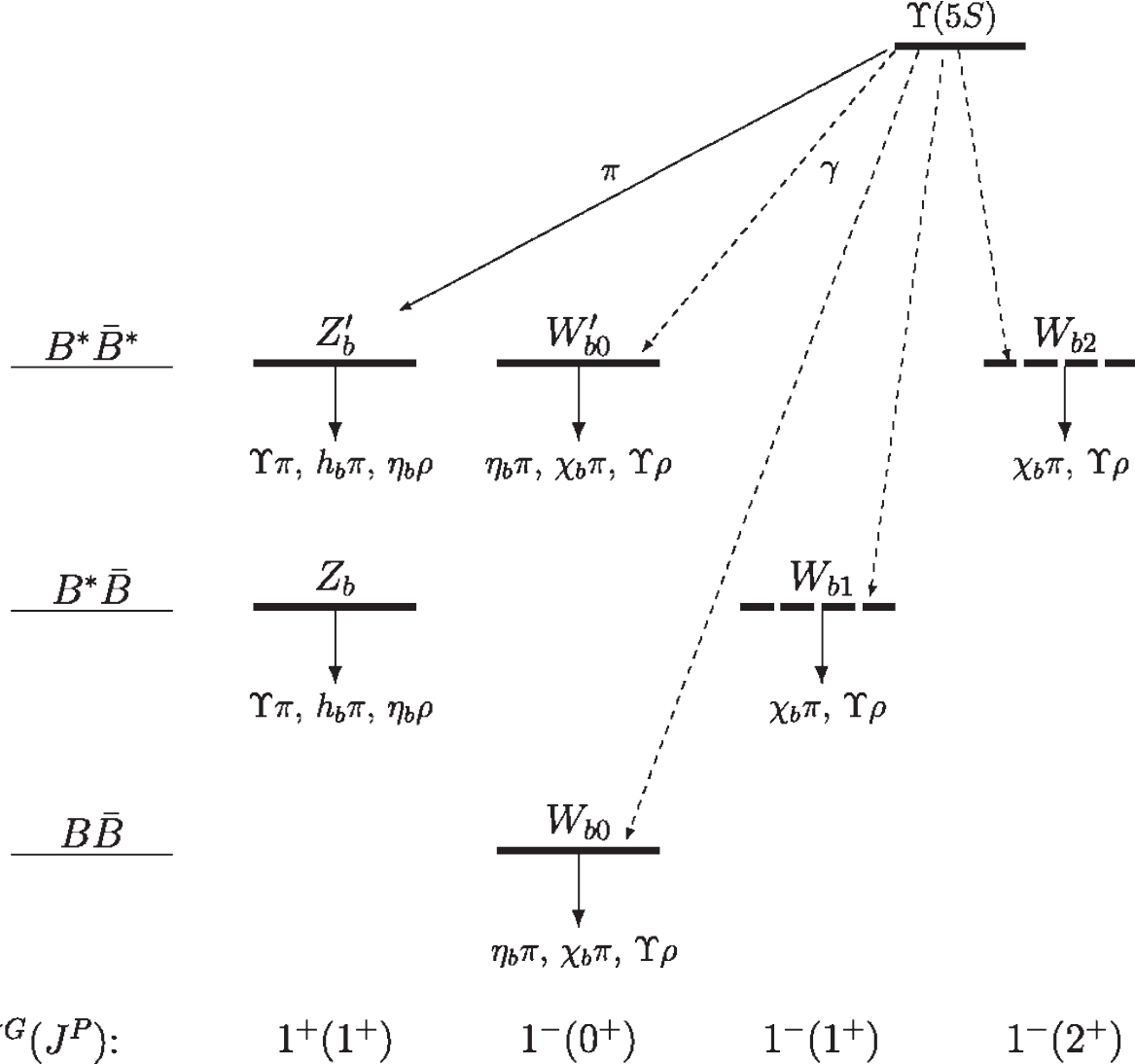


Figure 3: The expected family of isotriplet resonances from Ref. [13] (which the reader is advised to consult for relevant details). For $\Upsilon(6S)$ transitions, the photon is replaced by ρ . This would also allow to access charged W_{bJ} states. Also, please see Table 1.

174 driven by hope that nature might be kinder to us than we deserve. Also, tangentially, our
 175 LHC colleagues have been searching for signatures of SUSY for some time already, and, no
 176 matter how little has been observed so far, their noble quest will stop not. So why should we
 177 stop ours? On this philosophical note we conclude this discussion and proceed to describe
 178 our actual analysis.

179 2 Monte Carlo and Data Samples

180 To study the properties of signal events, we generate 100,000 Monte Carlo (MC) events
 181 for $\Upsilon(5S) \rightarrow \gamma W_{bJ}$ followed by $W_{bJ} \rightarrow \Upsilon(1S)\rho^0$, $\Upsilon(1S) \rightarrow \mu^+\mu^-$, $\rho^0 \rightarrow \pi^+\pi^-$ using MC
 182 generator EvtGen [16]. Detector response is simulated using GEANT4 [17]. W_{bJ} is generated

183 with an intrinsic width of 15 MeV, similar to the widths of Z_b and Z'_b . Table 2 displays the
 184 decay models [18] used in MC simulation of signal processes. The PHOTOS package [19] is
 185 used to simulated final state radiation (FSR). To allow for softer FSR photons in simulation,
 186 we modified the PHOTOS package to lower the minimum energy of final state radiation.
 187 Please see Section 10.1 for details.

188 We use six streams of generic MC to study background events. Each stream is equivalent
 189 to a full Belle data sample of 121.4 fb^{-1} of $\Upsilon(5S)$ resonance data. We generate additional MC
 190 samples to study background events originating from $\Upsilon(5S) \rightarrow \Upsilon(1S)\pi^+\pi^- \rightarrow \mu^+\mu^-\pi^+\pi^-$
 191 with initial state radiation (ISR) as well as events originating from $\Upsilon(5S) \rightarrow Z_b^\pm\pi^\mp \rightarrow$
 192 $\Upsilon(1S)\pi^\pm\pi^\mp \rightarrow \mu^+\mu^-\pi^\pm\pi^\mp$. We describe or studies of these processes in Section 6 and
 193 Section 7, respectively.

194 In this analysis, we use the full 121.4 fb^{-1} of on-resonance $\Upsilon(5S)$ data collected by the
 195 Belle detector at the KEKB collider from asymmetric energy e^+e^- collisions with $\sqrt{s} = 10.86$
 196 GeV [20].

Decay Process	Decay Model used in Mote Carlo Simulation
$\Upsilon(5S) \rightarrow W_{bJ}\gamma$	VSP_PWAVE
$W_{bJ} \rightarrow \Upsilon(1S)\rho^0$	SVV_HELAMP
$\rho^0 \rightarrow \pi^+\pi^-$	VSS
$\Upsilon(1S) \rightarrow \mu^+\mu^-$	VLL
Final state radiation	PHOTOS (modified)

Table 2: EvtGen decay models used in Mote Carlo simulation of signal processes.

197 3 Selection Criteria

198 We reconstruct the decay mode $\Upsilon(5S) \rightarrow \gamma W_{bJ}$ followed by the decays $W_{bJ} \rightarrow \Upsilon(1S)\rho^0$,
 199 $\Upsilon(1S) \rightarrow \mu^+\mu^-$, $\rho^0 \rightarrow \pi^+\pi^-$. We select a fully-reconstructed final state particle combination
 200 consisting of $\pi^+\pi^-\mu^+\mu^-\gamma$.

201 3.1 Selection of Photon Candidates

202 We require reconstructed photons have energy between 100 and 600 MeV and polar angle
 203 between 17° and 150° . In the center of mass reference frame, the radiative photon is expected
 204 to be monochromatic with energy of approximately 300 MeV. To reject showers produced by
 205 neutral hadrons, we require $E_9/E_{25} > 0.75$, where the E_9/E_{25} ratio is defined as the energy
 206 summed in the 3 x 3 array of crystals surrounding the center of the shower (E_9) to that of
 207 the 5 x 5 array of crystals surrounding the center of the shower (E_{25}).

208 3.2 Selection of Pion and Muon Candidates

209 Pion candidates must satisfy $R_{K,\pi} < 0.9$, where $R_{K,\pi}$ is the ‘‘Kaon identification variable’’
 210 defined as the likelihood ratio of the charged track to be due to a kaon versus a pion, and

Particle Candidate	Selection Criteria
γ	$100 < \text{MeV } E(\gamma) < 600 \text{ MeV}$
π^\pm, μ^\pm	$dr < 0.3 \text{ cm}$ $ dz < 2 \text{ cm}$ $p_T > 100 \text{ MeV}/c$
π^\pm PID	$R_{K,\pi} < 0.9$ $R_{e,\text{hadron}} < 0.9$
μ^\pm	$R_\mu > 0.10$
ρ^0	$0.420 \text{ GeV}/c^2 < M_{\pi^+\pi^-} < 1.020 \text{ GeV}/c^2$
$\Upsilon(1S)$	$9.3 \text{ GeV}/c^2 < M_{\mu^+\mu^-} < 9.6 \text{ GeV}/c^2$
$\Upsilon(5S)$	$10.2 \text{ GeV}/c^2 < M_{\pi^+\pi^-\mu^+\mu^-\gamma} < 11.5 \text{ GeV}/c^2$ $-0.05 \text{ GeV} < \Delta E < 0.03 \text{ GeV}$
(full event reconstruction)	Exactly four tracks: two muons and two pions

Table 3: Selection criteria for $\Upsilon(5S) \rightarrow \gamma W_{bJ}$

211 $R_{e,\text{hadron}} < 0.9$, where $R_{e,\text{hadron}}$ is the likelihood ratio of the charged track to be due to
212 an electron versus a hadron. Similarly, muon candidates must satisfy $R_\mu > 0.1$, where
213 R_μ is the likelihood ratio of the charged track to be due to a muon versus other particles
214 detected by the KLM detector subsystem. After imposing the aforementioned requirements,
215 we additionally require there to be four unique charged tracks – two pions and two muons.
216 Events with more than four such tracks are rejected.

217 To select reconstructed track that originate near the interaction point, we require pion
218 and muon candidates have $dr < 0.3 \text{ cm}$ and $|dz| < 2 \text{ cm}$, where dr and dz are impact
219 parameters in the radial and z directions, respectively. We also require pion and muon
220 candidates to have transverse momenta $p_T > 100 \text{ MeV}$. Candidate muon pairs must have
221 an invariant mass between $9.3 \text{ GeV}/c^2$ and $9.6 \text{ GeV}/c^2$. Candidate pion pairs must have an
222 invariant mass between $0.42 \text{ GeV}/c^2$ and $1.02 \text{ GeV}/c^2$.

223 3.3 Selection of $\Upsilon(5S)$ Candidates

224 $\Upsilon(5S)$ candidates are required to have an invariant mass between 10.2 GeV and 11.5 GeV .
225 The muon pairs of selected $\Upsilon(5S)$ candidates are mass constrained to the nominal $\Upsilon(1S)$
226 invariant mass of $9.460 \text{ GeV}/c^2$. A summary of our selection criteria is shown in Table 3.

227 3.4 Best Candidate Selection

228 Approximately 32% of signal MC events satisfying our selection criteria have multiple signal
229 candidates. This is exclusively due to relatively soft photons. In events with multiple signal
230 candidates, we select the candidate that has an energy most consistent with the center of
231 mass energy of the experimental run. The selected candidates are correctly MC-tagged to full

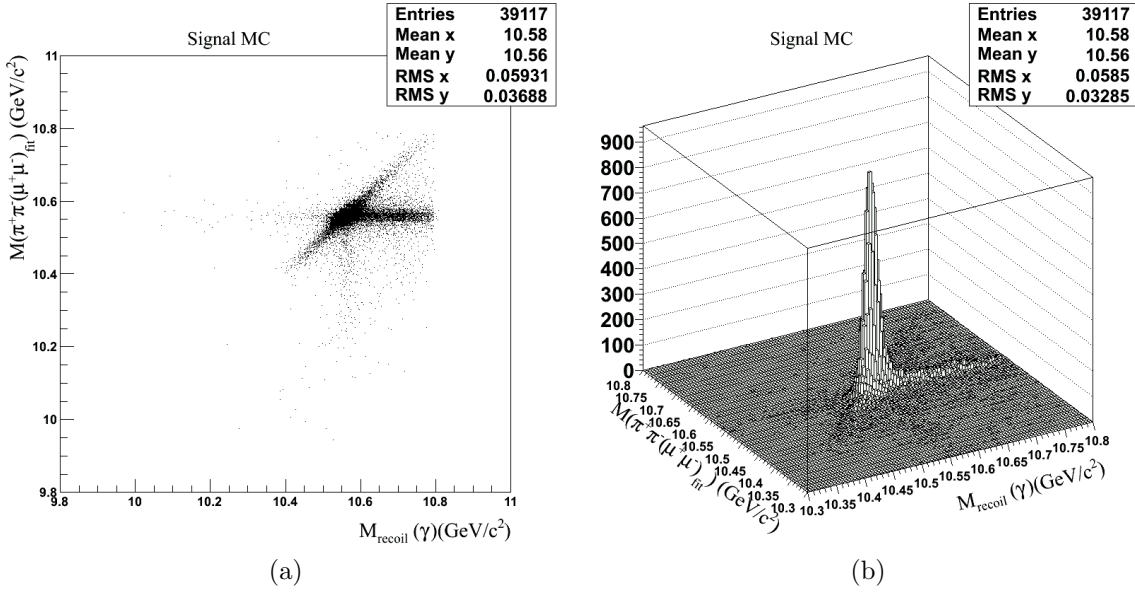


Figure 4: $M(\pi^+\pi^-(\mu^+\mu^-)_{\text{fit}})$ vs $M_{\text{rec}}(\gamma)$ distribution for W_{B0} signal MC events. We show the lego plot in Fig. 4b to emphasize that the tail of $M_{\text{rec}}(\gamma)$ is not as large as it appears in Fig. 4a. Note that Fig. 4b is plotted in a smaller range.

Quantity	Value
Intrinsic width of W_{bJ}	15 MeV/ c^2
Charged track resolution	4 MeV
Photon energy resolution	8 MeV
Beam energy resolution	6 MeV

Table 4: Quantities contributing to widths of measured quantities

232 MC truth for signal 90% of the time. For fully reconstructed signal MC events with multiple
 233 candidates, our best candidate selection method selects a candidate correctly MC-tagged to
 234 full MC truth 88% of the time.

235 4 Signal Monte Carlo Studies

236 4.1 Signal Monte Carlo Distributions

237 To understand properties of signal events, we investigate two invariant mass variables,
 238 $M(\pi^+\pi^-(\mu^+\mu^-)_{\text{fit}})$ and $M_{\text{rec}}(\gamma)$, where subscript "fit" indicates that the muon pair is con-
 239 strained to the nominal mass of $\Upsilon(1S)$. We define the invariant mass recoiling against X
 240 as

$$M_{\text{rec}}(X) = \sqrt{(E_{\text{cm}}(\text{exp}) - E_{\text{cm}}(X))^2 - |\vec{0} - \vec{p}_{\text{cm}}(X)|^2} \quad (2)$$

241 where $E_{\text{cm}}(\text{exp})$ is the run’s average energy, and $E_{\text{cm}}(X)$ and $\vec{p}_{\text{cm}}(X)$ are the energy and
 242 momentum of system X . Subscript “cm” is used for quantities evaluated in the center of
 243 mass reference frame of the experiment. For signal events, $M_{\text{recoil}}(\gamma)$ and $M(\pi^+\pi^-(\mu^+\mu^-)_{\text{fit}})$
 244 are two independent ways to estimate the invariant mass of W_{bJ} . Fully reconstructed signal
 245 events fall along the main diagonal of the $M(\pi^+\pi^-(\mu^+\mu^-)_{\text{fit}})$ vs $M_{\text{rec}}(\gamma)$ plot shown in Fig. 4.
 246 We define energy balance ΔE as

$$\Delta E = E_{\text{cm}}(\pi^+\pi^-(\mu^+\mu^-)_{\text{fit}}\gamma) - E_{\text{cm}}(\text{exp}). \quad (3)$$

247 ΔE is the most important variable we can use to select fully reconstructed signal event
 248 candidates.

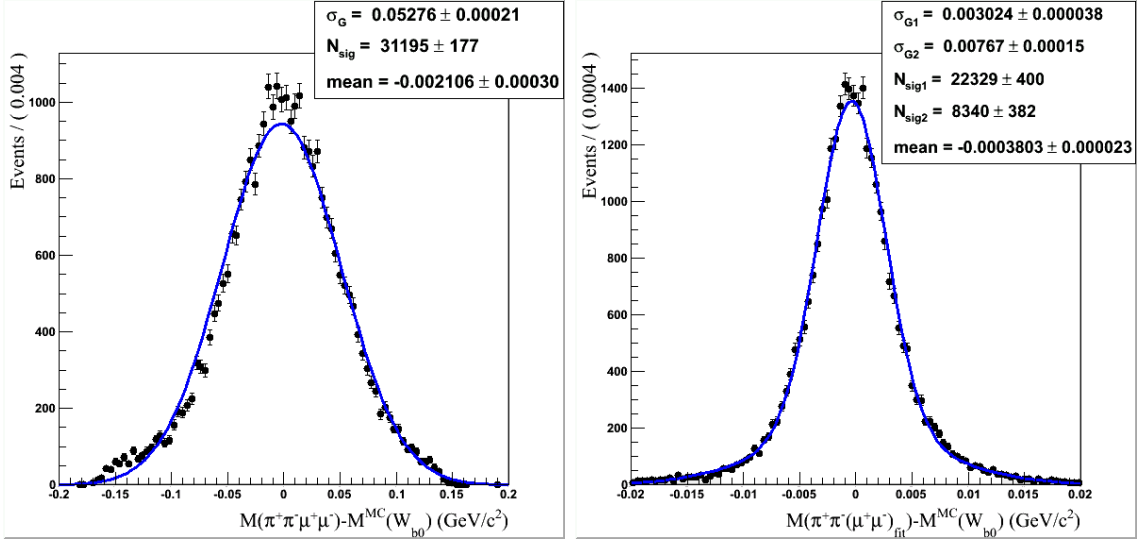
249 There are two effects contributing to the observed width of $M(\pi^+\pi^-(\mu^+\mu^-)_{\text{fit}})$: (1) the
 250 intrinsic width of W_{bJ} , and (2) the charged track reconstruction. Fig. 5 shows $M(\pi^+\pi^+\mu^+\mu^-)$
 251 and $M(\pi^+\pi^-(\mu^+\mu^-)_{\text{fit}})$ resolutions for signal events within the signal region and sideband
 252 regions (defined in Section 4.2). We model both resolutions as the sum of two Gaussians
 253 with the same mean and fit both resolutions. Contribution to $M(\pi^+\pi^-(\mu^+\mu^-)_{\text{fit}})$ resolution
 254 from charged track reconstruction is primarily due to pions, since muon pairs are constrained
 255 to $\Upsilon(1S)$ invariant mass.

256 The distribution of $M_{\text{rec}}(\gamma)$ has a long tail due to an underestimation of photon energy,
 257 causing an overestimation of $M_{\text{rec}}(\gamma)$. Effects contributing to the observed width of $M_{\text{rec}}(\gamma)$
 258 include (1) intrinsic width of W_{bJ} , and (2) photon energy resolution. $M_{\text{rec}}(\gamma)$ resolution is
 259 dominated by photon energy resolution.

260 Effects contributing to the observed shape of ΔE include (1) photon energy resolution, (2)
 261 charged track resolution, (3) beam energy resolution, and (4) the intrinsic width of W_{bJ} . ΔE
 262 resolution is dominated by photon energy resolution as well. The values of relevant widths
 263 are listed in Table 4. In signal MC we observe $\sigma_{\Delta E} \approx 12$ MeV, so we take advantage of this
 264 excellent energy resolution to select fully reconstructed events. Because the distribution of
 265 ΔE is asymmetric (primarily due to leakage from the calorimeter and relatively soft non-
 266 signal photons in signal events), we use an asymmetric selection and require $-0.05 \text{ GeV} \leq$
 267 $\Delta E \leq 0.03 \text{ GeV}$. This selection cuts out the long tail in the distribution of $M_{\text{rec}}(\gamma)$ and
 268 reduces the efficiency by 20%. Note, however, that this selection primarily removes events
 269 where the signal photon is not reconstructed. After applying this selection on ΔE , signal
 270 reconstruction efficiency becomes approximately 31%. Fig. 6 displays ΔE resolution as well
 271 as quantities contributing to ΔE resolution.

272 4.2 Description of the Signal Region

273 Table 5 contains the definitions of four important regions in this analysis. Before investigating
 274 data, we blind the region where we expect to find signal. We refer to this region as the
 275 blinded region. The invariant masses of W_{b0} , W_{b1} , and W'_{b0} and W_{b2} are expected to be at
 276 the $B\bar{B}$, $B^*\bar{B}$, and $B^*\bar{B}^*$ thresholds, respectively. The blinded region is defined as the region
 277 between the $B\bar{B}$ and $B^*\bar{B}^*$ thresholds plus an additional margin of 70 MeV on either side.
 278 This corresponds to $10.49 \text{ GeV}/c^2 \leq M(\pi^+\pi^-(\mu^+\mu^-)_{\text{fit}}) \leq 10.72 \text{ GeV}/c^2$. The boundary on
 279 the left side of the region is defined by the sloped line $M_{\text{rec}}(\gamma) \geq M(\pi^+\pi^-(\mu^+\mu^-)_{\text{fit}}) - 0.04$
 280 GeV/c^2 which lies parallel to the main diagonal. Approximately 20% of signal events are



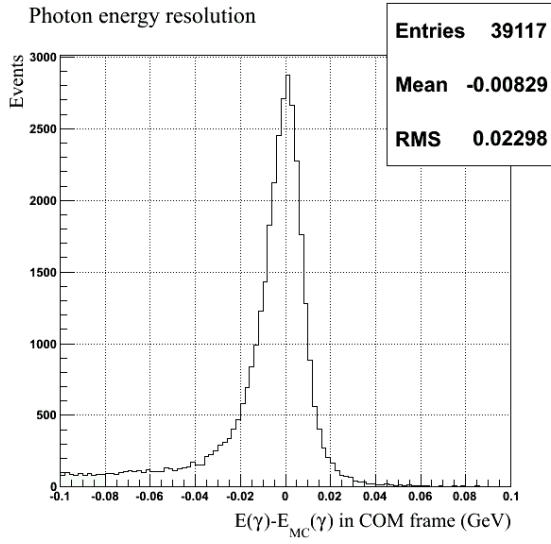
(a) $M(\pi^+\pi^+\mu^+\mu^-)$ resolution. Note that muons are not mass constrained. (b) $M(\pi^+\pi^-(\mu^+\mu^-)_{\text{fit}})$ resolution (muons are mass constrained).

Figure 5: $M(\pi^+\pi^+\mu^+\mu^-)$ and $M(\pi^+\pi^-(\mu^+\mu^-)_{\text{fit}})$ resolutions for signal events within the signal region and sideband regions (defined in Section 4.2). Note that the horizontal scales are different.

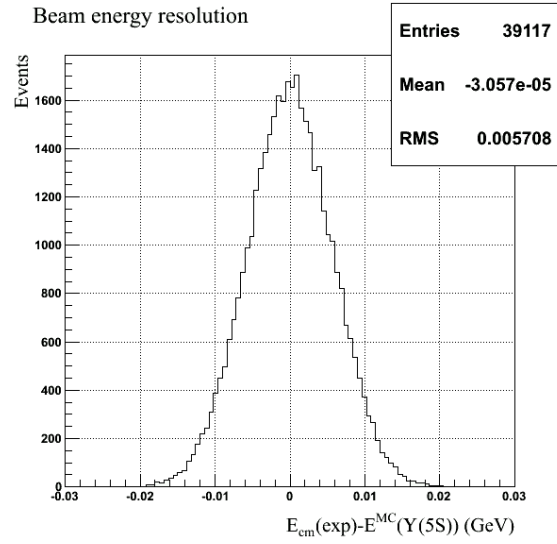
Region Name	Boundary Definitions
Blinded Region	$10.49 \text{ GeV}/c^2 \leq M(\pi^+\pi^-(\mu^+\mu^-)_{\text{fit}}) \leq 10.72 \text{ GeV}/c^2$ $M_{\text{rec}}(\gamma) \geq M(\pi^+\pi^-(\mu^+\mu^-)_{\text{fit}}) - 0.04 \text{ GeV}/c^2$ $M_{\text{rec}}(\gamma) \leq 10.8 \text{ GeV}/c^2$
Signal Region	$10.49 \text{ GeV}/c^2 \leq M(\pi^+\pi^-(\mu^+\mu^-)_{\text{fit}}) \leq 10.72 \text{ GeV}/c^2$ $-0.05 \text{ GeV} \leq \Delta E \leq 0.03 \text{ GeV}$
Sideband Region	$10.38 \text{ GeV}/c^2 \leq M(\pi^+\pi^-(\mu^+\mu^-)_{\text{fit}}) \leq 10.49 \text{ GeV}/c^2$ $10.72 \text{ GeV}/c^2 \leq M(\pi^+\pi^-(\mu^+\mu^-)_{\text{fit}}) \leq 10.80 \text{ GeV}/c^2$ $-0.05 \text{ GeV} \leq \Delta E \leq 0.03 \text{ GeV}$.
Grand Sideband Region	$10.38 \text{ GeV}/c^2 \leq M(\pi^+\pi^-(\mu^+\mu^-)_{\text{fit}}) \leq 10.80 \text{ GeV}/c^2$ $-0.20 \text{ GeV} \leq \Delta E \leq 0.20 \text{ GeV}$

Table 5: Definitions of the signal region and other important regions.

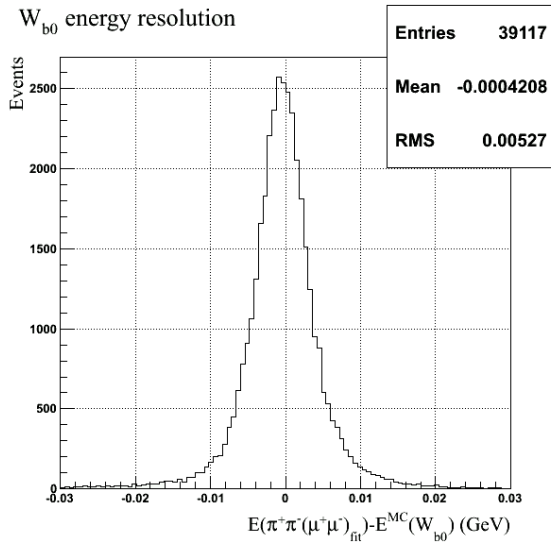
281 located in the long right tail of the distribution of $M_{\text{rec}}(\gamma)$. A phase space boundary on
282 the right side of the plot at $M_{\text{rec}}(\gamma) \approx 10.75 \text{ GeV}/c^2$ forces this long tail of the $M_{\text{rec}}(\gamma)$
283 distribution into a smaller region for the higher mass W_{bJ} states. Hence, we do not define
284 a sloped boundary line as the right side of the signal region – a diagonal boundary would
285 exclude more signal events for the lower mass states because of the aforementioned phase
286 space boundary compressing the tail. Instead, we define the vertical line boundary $M_{\text{rec}}(\gamma) \leq$



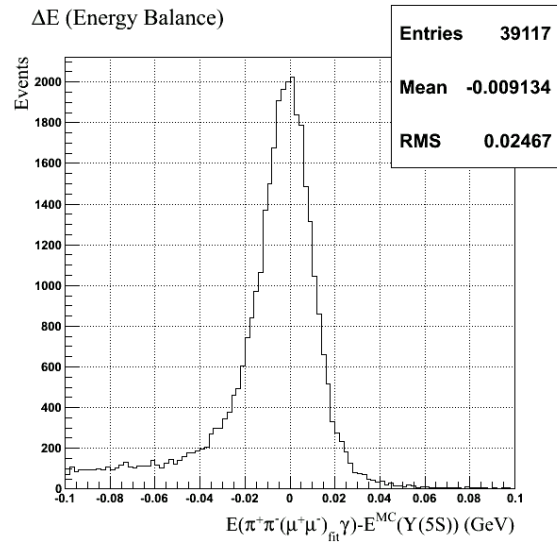
(a) Signal photon energy line shape in the COM reference frame.



(b) Beam energy resolution.



(c) $M(\pi^+\pi^-(\mu^+\mu^-)_{\text{fit}})$ energy line shape (includes the effect of intrinsic W_{bJ} width and charged track reconstruction).



(d) Signal candidate energy line shape. Includes the effects of W_{bJ} intrinsic width and resolution.

Figure 6: ΔE resolution and quantities contributing to ΔE resolution.

287 $10.72 \text{ GeV}/c^2$ which assures that approximately equal percentages of signal would be blinded
 288 for all masses of W_{bJ} states.

289 We define the signal region as the region contained within $10.49 \text{ GeV}/c^2 \leq M(\pi^+\pi^-(\mu^+\mu^-)_{\text{fit}}) \leq$
 290 $10.72 \text{ GeV}/c^2$ satisfying $-0.05 \text{ (GeV)} \leq \Delta E \leq 0.03 \text{ GeV}$. The ΔE requirement selects only
 291 fully-reconstructed signal events, where signal is peaking.

292 The sideband region is essentially an extension of the signal region, defined as the
 293 regions within $10.38 \text{ GeV}/c^2 \leq M(\pi^+\pi^-(\mu^+\mu^-)_{\text{fit}}) \leq 10.49 \text{ GeV}/c^2$ and $10.72 \text{ GeV}/c^2 \leq$

294 $M(\pi^+\pi^-(\mu^+\mu^-)_{\text{fit}}) \leq 10.80 \text{ GeV}/c^2$ satisfying $-0.05 \text{ (GeV)} \leq \Delta E \leq 0.03 \text{ GeV}$.

295 We additionally define the grand sideband region as the region within $10.38 \text{ GeV}/c^2 \leq$
 296 $M(\pi^+\pi^-(\mu^+\mu^-)_{\text{fit}}) \leq 10.80 \text{ GeV}/c^2$ satisfying $-0.20 \text{ GeV} \leq \Delta E \leq 0.20 \text{ GeV}$. This region is
 297 used when studying background in data.

298 Fig. 7 displays these four regions with our three signal MC samples. It is important to
 299 note that the blinded region is not completely contained within the grand sideband region
 300 and the signal region is not completely contained within the blinded region. This is due to
 301 historical reasons, as the blinded region was defined prior to the use of ΔE in this analysis.

302 4.3 Trigger Simulation

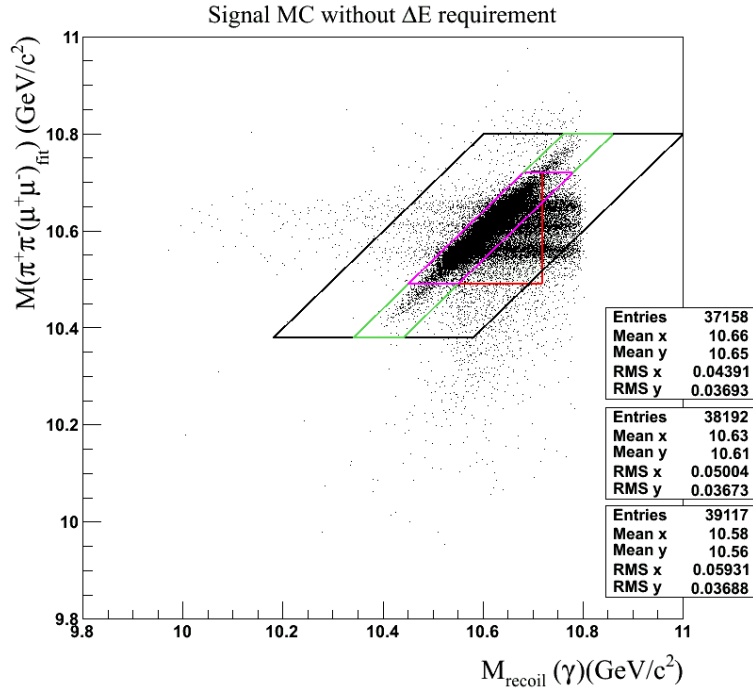
303 Relatively low final state particle multiplicity of our signal events requires us to investigate
 304 trigger efficiency. Trigger efficiency is simulated after full reconstruction. We find correlations
 305 between trigger efficiency and kinematics. Fig. 8 shows various 2-dimensional distributions
 306 of $\mu^+ \cos(\theta)$ vs $\mu^+ \cos(\theta)$, and we see that events failing to satisfy trigger are more likely to
 307 have one of the muons at a small angle with respect to the beam axis ($|\cos(\theta)| \geq 0.8$). Fig. 9
 308 shows additional distributions of $\mu^+ \cos(\theta)$ vs $\mu^+ \cos(\theta)$ which we use to determine trigger
 309 efficiencies. When neither muon is at a small angle with respect to the beam axis, trigger
 310 efficiency is 96%. When one of the muons is at a small angle with respect to the beam
 311 axis, trigger efficiency drops to 89%. For all generated signal MC events, trigger efficiency is
 312 approximately 94%. After accounting for trigger efficiency, our overall efficiency drops from
 313 31% to 29%.

314 5 Background Studies

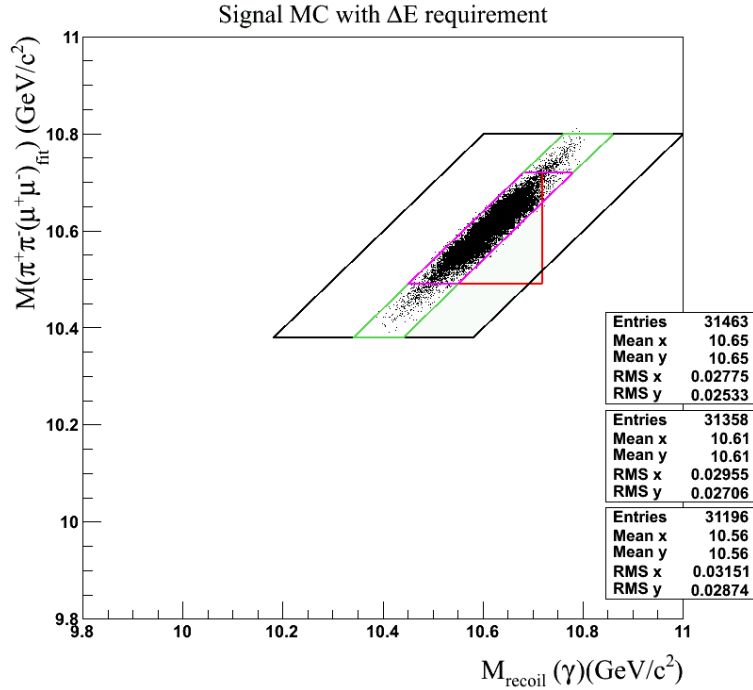
315 5.1 Generic Monte Carlo and Blinded Data

316 Fig. 10 shows the distribution of $M(\pi^+\pi^-(\mu^+\mu^-)_{\text{fit}})$ vs $M_{\text{rec}}(\gamma)$ for generic MC and blinded
 317 data events. Using MC truth, we identify the background decays in generic MC and blinded
 318 data and group them into eight categories which are defined in Table 6. No uds , charm,
 319 or $B_s B_s$ generic MC events pass our selection criteria. A large number of non- $B_s B_s$ events
 320 do satisfy our selection criteria, though they fall primarily outside the signal region. The
 321 ΔE requirement excludes most of these background events. The most prominent non- $B_s B_s$
 322 background sources are (cascade) dipion transitions to $\Upsilon(1S)$. We observe an enhancement
 323 in generic MC within the blinded region due to the decay $\Upsilon(5S) \rightarrow \Upsilon(2S)\pi^+\pi^-$, $\Upsilon(2S) \rightarrow$
 324 $\Upsilon(1S)\pi^+\pi^-$ where the selected signal pion candidates did not come from the same parent.
 325 The enhancement is removed when the ΔE constraint is applied, as such background events
 326 are not fully reconstructed.

327 We observe several regions where data events are clustering but generic MC events are
 328 not, and we have identified the likely origins of these events. The regions labeled X and Z
 329 in Fig. 10 are populated by events which are due to radiative returns to a lower mass $\Upsilon(nS)$
 330 where the radiative photon is selected as our signal photon candidate. These events are
 331 fully reconstructed, and thus fall along the main diagonal of the plot. The region labeled
 332 Y includes processes involving radiative decays of $\chi_{bJ}(1P)$. These events have additional



(a) Does not include ΔE requirement.



(b) Includes ΔE requirement.

Figure 7: The blinded region (red), signal region (magenta), sideband region (green), and the grand sideband region (black). The plot in 7a includes the aforementioned ΔE requirement, while the plot in 7b does not. From top to bottom, the statistics boxes correspond to W'_{b0} , W_{b1} , and W_{b0} signal MC, respectively.

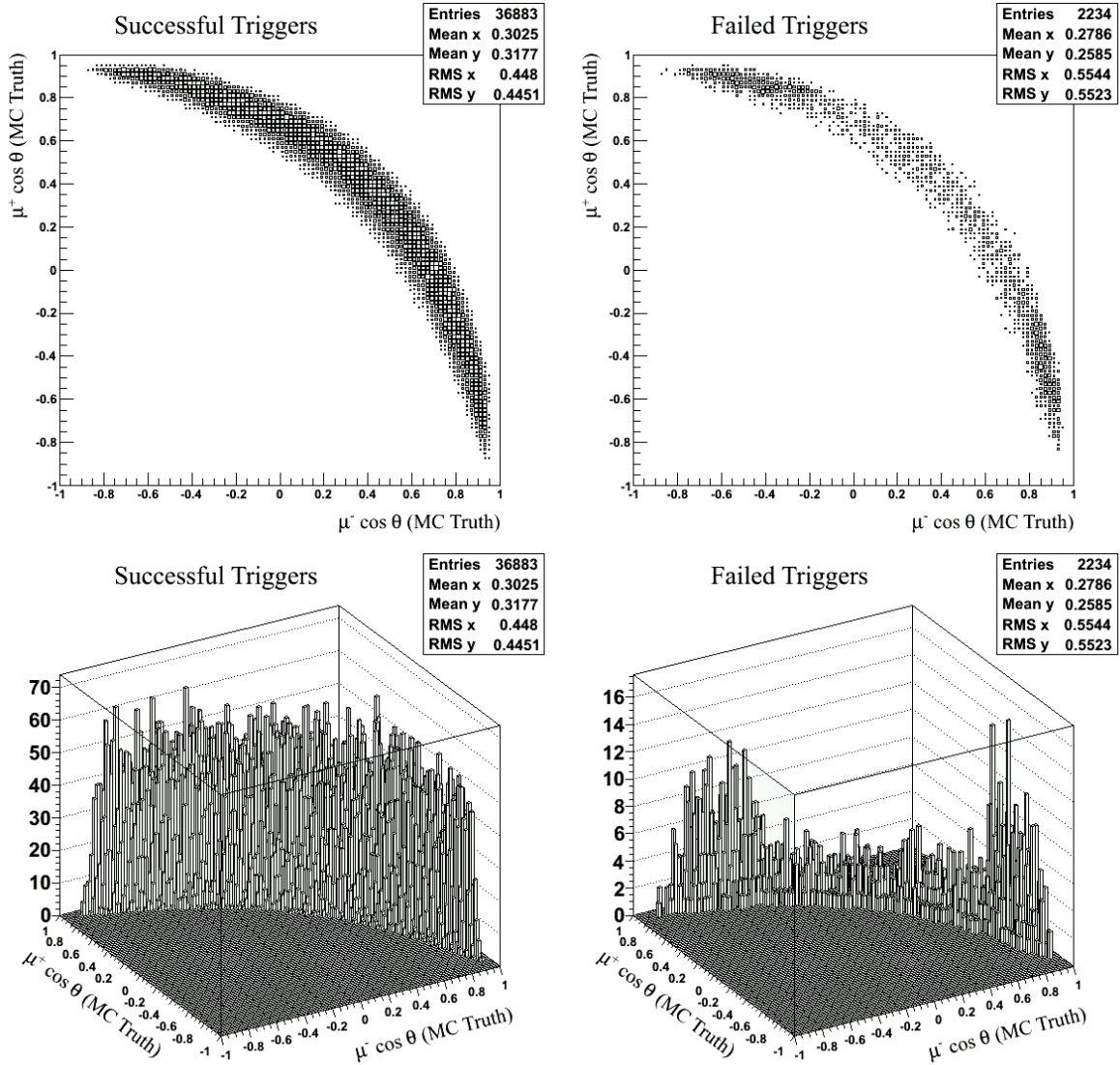


Figure 8: Reconstructed signal MC events that satisfy the offline trigger selection are plotted on the left, while events that fail the offline trigger selection are plotted on the right. We observe that events satisfying the trigger criteria are distributed more or less uniformly for kinematically allowed muons, but events failing to satisfy trigger are more likely to have one of the muons at a small angle with respect to the beam axis.

333 final state particles that are not reconstructed, and hence they fall below the main diagonal
 334 where $\Delta E < 0$. Events in categories X, Y, and Z are not of concern to us, since they are
 335 located far from the signal region.

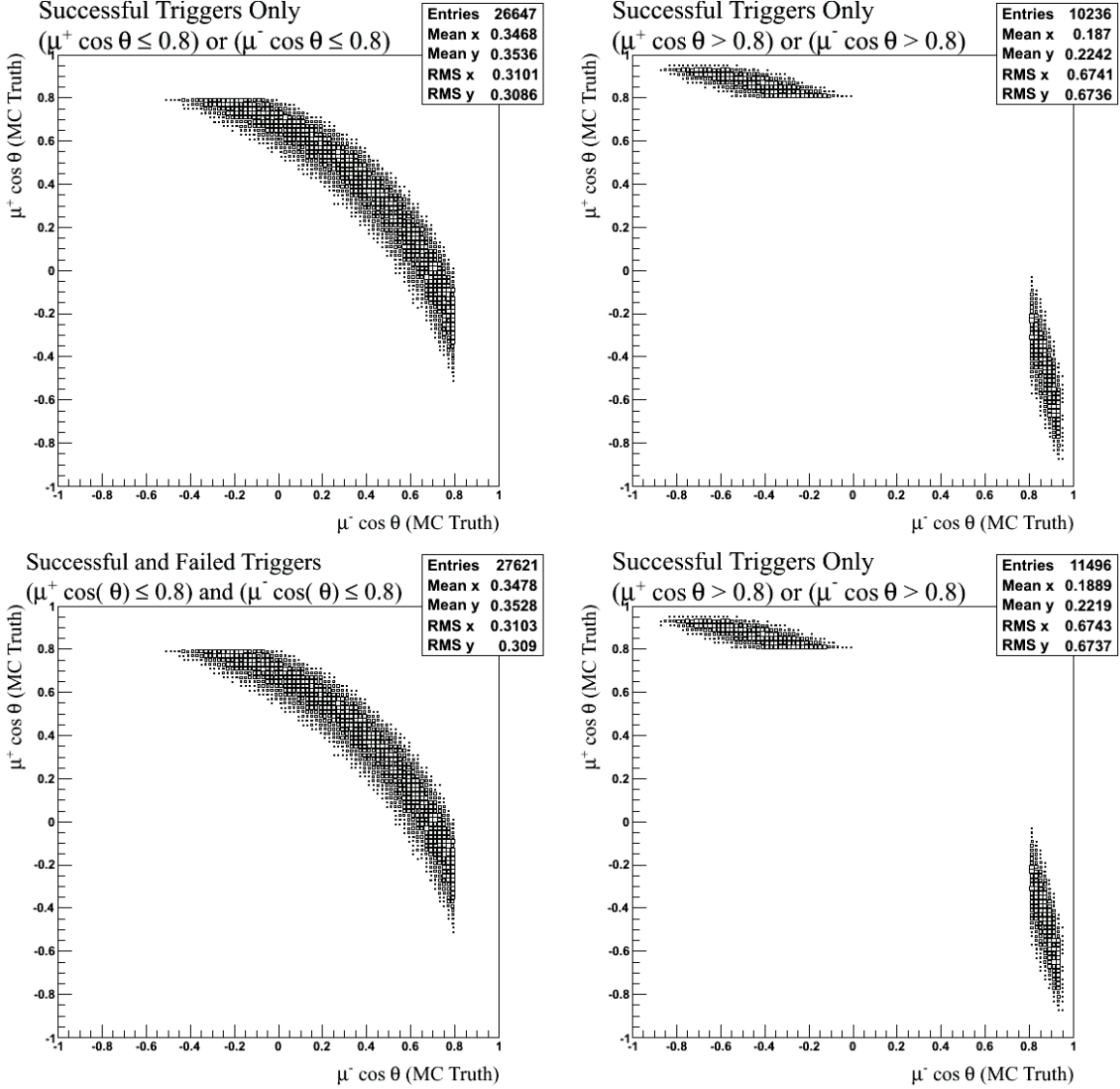


Figure 9: All reconstructed events in which both muons are generated with $|\cos(\theta)| < 0.8$ are plotted in the left two figures. Trigger efficiency for such events is approximately $(96 \pm 4)\%$. In the right two figures, we plot all reconstructed events where one of the muons is generated with $|\cos(\theta)| > 0.8$. Trigger efficiency for these events is reduced to about $(89 \pm 4)\%$.

336 6 Background from $\Upsilon(5S) \rightarrow \Upsilon(1S)\pi^+\pi^-$ with Initial 337 State Radiation (ISR)

338 We find that dipion transitions to $\Upsilon(1S)$ (labeled 'A' in Fig. 10) have a much longer tail
339 in data than in generic MC. This difference is shown in Fig. 11, and is due to initial state
340 radiation (ISR). This tail contaminates the signal region, so we generate additional MC
341 samples with ISR to study these backgrounds.

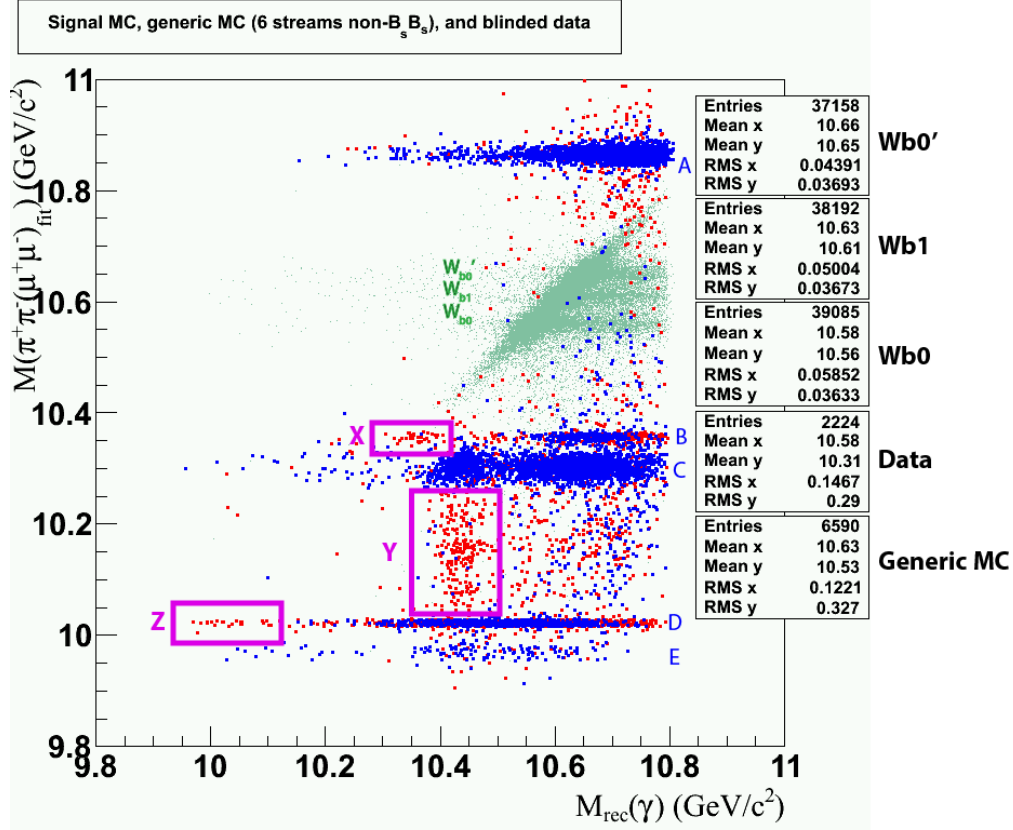


Figure 10: W_{b0} , W_{b1} , and W'_{b0} signal MC (light green), six streams of non- $B_s B_s$ generic MC (blue), and data with the signal region blinded (red).

Label	Background
A	$\Upsilon(5S) \rightarrow \Upsilon(1S)\pi^+\pi^- \rightarrow \mu^+\mu^-\pi^+\pi^-$
B	$\Upsilon(5S) \rightarrow \Upsilon(3S)\pi^+\pi^- \rightarrow \Upsilon(1S)\pi^+\pi^-\pi^+\pi^- \rightarrow \mu^+\mu^-\pi^+\pi^-\pi^+\pi^-$ $\Upsilon(5S) \rightarrow \Upsilon(3S)\pi^0\pi^0 \rightarrow \Upsilon(1S)\pi^+\pi^-\pi^0\pi^0 \rightarrow \mu^+\mu^-\pi^+\pi^-\pi^0\pi^0$
C	$\Upsilon(5S) \rightarrow \Upsilon(2S)\pi^+\pi^- \rightarrow \Upsilon(1S)\pi^+\pi^-\pi^+\pi^- \rightarrow \mu^+\mu^-\pi^+\pi^-\pi^+\pi^-$ $\Upsilon(5S) \rightarrow \Upsilon(2S)\pi^+\pi^- \rightarrow \Upsilon(1S)\pi^0\pi^0\pi^+\pi^- \rightarrow \mu^+\mu^-\pi^0\pi^0\pi^+\pi^-$
D	$\Upsilon(5S) \rightarrow \Upsilon(2S)\pi^0\pi^0 \rightarrow \Upsilon(1S)\pi^+\pi^-\pi^0\pi^0 \rightarrow \mu^+\mu^-\pi^+\pi^-\pi^0\pi^0$
E	$\Upsilon(5S) \rightarrow \Upsilon(3S)\pi^+\pi^- \rightarrow \Upsilon(1S)\pi^0\pi^0\pi^+\pi^- \rightarrow \mu^+\mu^-\pi^0\pi^0\pi^+\pi^-$
X	$e^+e^- \rightarrow \Upsilon(3S)\gamma \rightarrow \Upsilon(1S)\pi^+\pi^-\gamma \rightarrow \mu^+\mu^-\pi^+\pi^-\gamma$
Y	Various processes involving $\chi_{bJ}(1P) \rightarrow \gamma\Upsilon(1S)$, <i>e.g.</i> $\Upsilon(5S) \rightarrow \Upsilon(1D)\pi^+\pi^-$, where $\Upsilon(1D) \rightarrow \gamma\chi_{bJ}(1P)$
Z	$e^+e^- \rightarrow \Upsilon(2S)\gamma \rightarrow \Upsilon(1S)\pi^+\pi^-\gamma \rightarrow \mu^+\mu^-\pi^+\pi^-\gamma$

Table 6: Backgrounds labeled in Fig. 10.

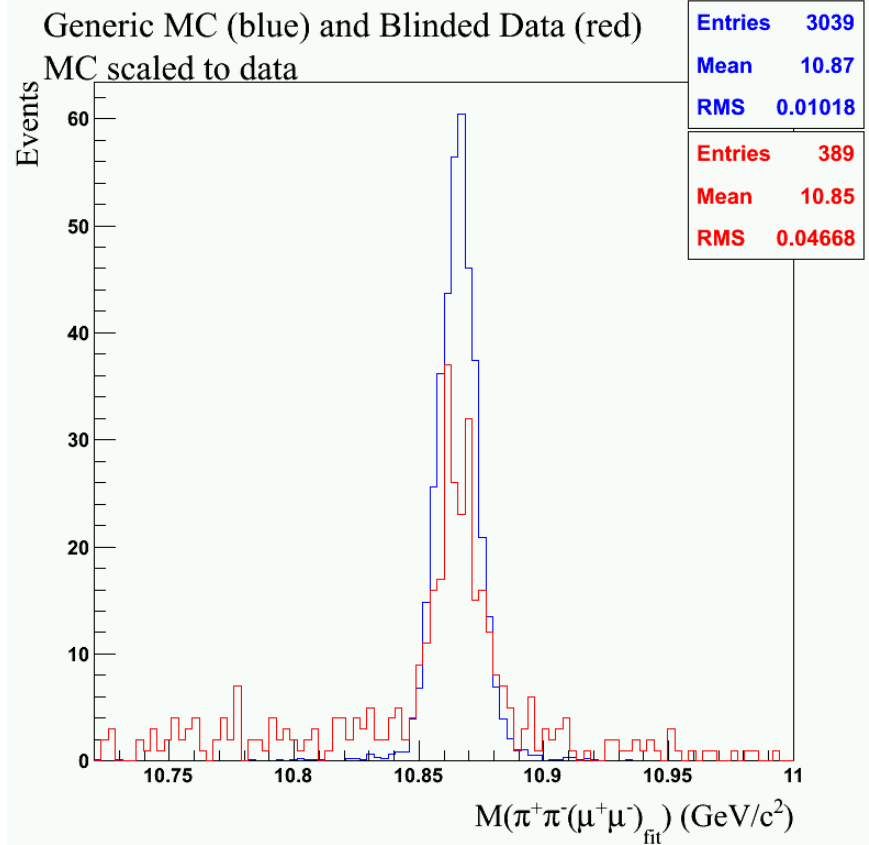


Figure 11: $M(\pi^+\pi^-(\mu^+\mu^-)_{\text{fit}})$ distributions for $\Upsilon(5S) \rightarrow \Upsilon(1S)\pi^+\pi^-$ events (label 'A' in Table 6). Distributions for generic MC and blinded data are shown in blue and red, respectively. Generic MC does not include ISR and is normalized to the number of data events shown in the plotted range. We choose $10.72 \text{ GeV}/c^2$ as the lower limit of the range plotted, since lower masses would include the blinded region.

342 6.1 $\Upsilon(5S) \rightarrow \Upsilon(1S)\pi^+\pi^-$ ISR Monte Carlo Sample

343 The VectorISR model [18] is used to simulate ISR. We reweight the ISR photon energy
 344 spectrum according to the correct radiator function up to order α^2 [21] using a Monte Carlo
 345 method. After reweighting, there are approximately 110,000 events in our MC sample. A
 346 distribution of the reweighted ISR spectrum is shown in Fig. 12.

347 Fig. 13 shows the $M(\pi^+\pi^-(\mu^+\mu^-)_{\text{fit}})$ vs $M_{\text{rec}}(\gamma)$ distribution for reweighted $\Upsilon(5S) \rightarrow$
 348 $\Upsilon(1S)\pi^+\pi^-$ events with ISR. Recall that the two plotted variables represent two independent
 349 ways to estimate the invariant mass of W_{bJ} , and therefore fully reconstructed events fall along
 350 the main diagonal of this plot. When the ISR photon of these backgrounds is selected as
 351 the signal photon candidate, these backgrounds are also fully reconstructed and fall along
 352 the main diagonal within the signal region. Approximately 3% of reconstructed events fall
 353 in the signal region. Fortunately, these backgrounds do not peak in the signal region in the
 354 distribution of $M(\pi^+\pi^-(\mu^+\mu^-)_{\text{fit}})$.

355 We simulate $\Upsilon(5S) \rightarrow \Upsilon(1S)\pi^+\pi^-$ with ISR using the models listed in Table 7. To
 356 determine if the choice of decay models affects the distribution shape of our signal variable

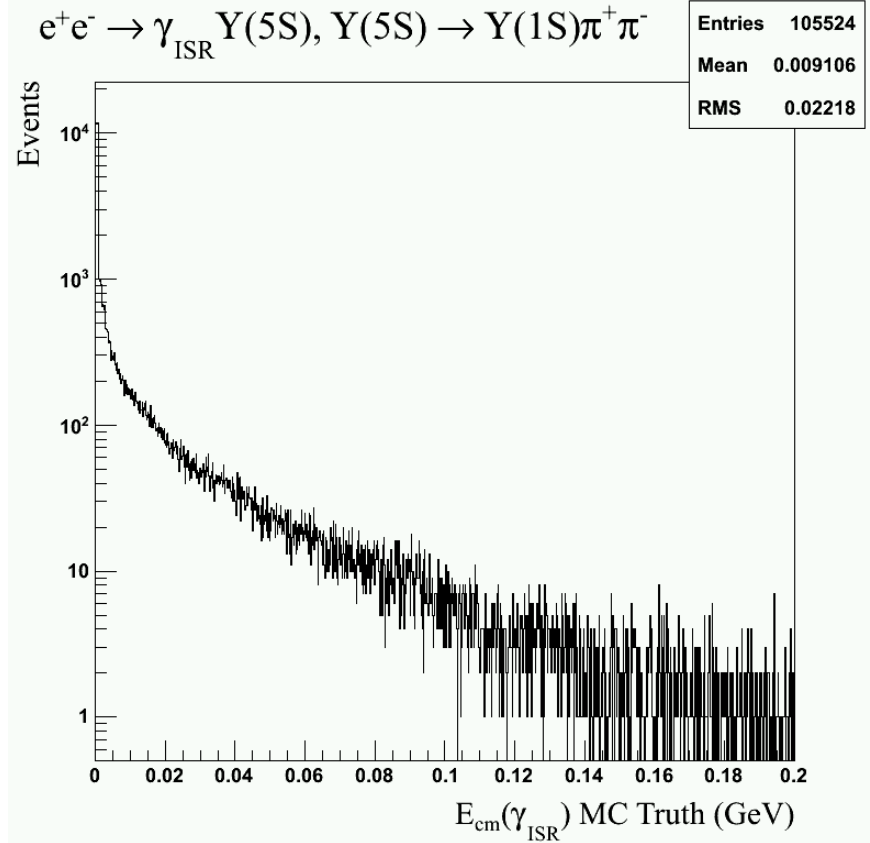


Figure 12: Reweighted ISR energy spectrum for $e^+e^- \rightarrow \gamma_{\text{ISR}}\Upsilon(5S), \Upsilon(5S) \rightarrow \Upsilon(1S)\pi^+\pi^-$. Note that a log scale is used for the vertical axis.

357 $M(\pi^+\pi^-(\mu^+\mu^-)_{\text{fit}})$, we generate additional samples using the VVPIPI decay [18] model for
 358 $\Upsilon(5S) \rightarrow \Upsilon(1S)\pi^+\pi^-$ and the VLL decay model [18] for $\Upsilon(1S) \rightarrow \mu^+\mu^-$. Fig. 14 shows the
 359 distribution of $M(\pi^+\pi^-(\mu^+\mu^-)_{\text{fit}})$ for two different MC samples generated using different
 360 decay models.

361 We find that the choice of decay model has only a small effect on the shape of the
 362 $M(\pi^+\pi^-(\mu^+\mu^-)_{\text{fit}})$ distribution. Furthermore, we plot the $\cos\theta$ of μ^+ in Fig. 15 and find
 363 that the presence of ISR has only a small effect on the the angular distributions of muons. To
 364 determine if ISR affects the width of the $M(\pi^+\pi^-(\mu^+\mu^-)_{\text{fit}})$ distribution for signal processes
 365 $\Upsilon(5S) \rightarrow \gamma W_{bJ}$, we generate additional MC samples for the the signal process $\Upsilon(5S) \rightarrow \gamma W_{bJ}$
 366 with ISR. We find that ISR has practically no effect on the width of the distribution of
 367 $M(\pi^+\pi^-(\mu^+\mu^-)_{\text{fit}})$.

368 6.2 Background Shape of $\Upsilon(5S) \rightarrow \Upsilon(1S)\pi^+\pi^-$ with ISR

369 It is likely that events due to $\Upsilon(5S) \rightarrow \Upsilon(1S)\pi^+\pi^-$ with ISR are a dominant source of
 370 backgrounds in the signal region. The rightmost plot in Fig. 16 shows the distribution of
 371 these events within the signal region for our reweighted MC. To see how the selection on
 372 ΔE affects the background shape, we loosen up the selection on ΔE in the left and middle
 373 plots in Fig. 16. Imposing a selection on ΔE has only a small effect on the shape of these

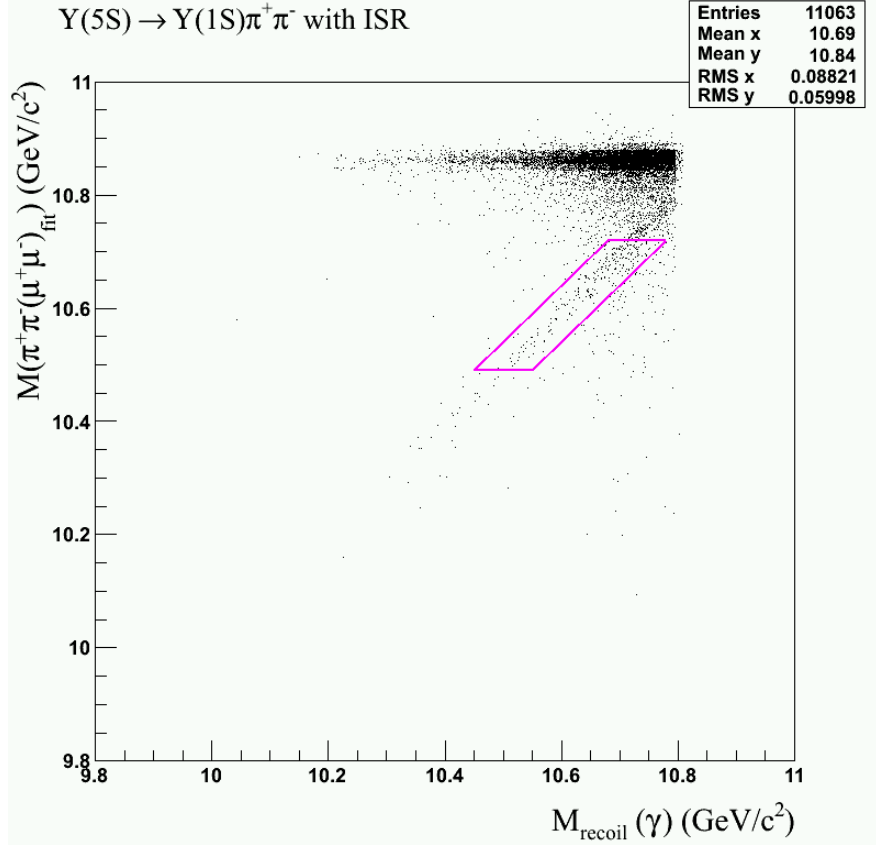


Figure 13: A 2-dimensional $M(\pi^+\pi^-(\mu^+\mu^-)_{\text{fit}})$ vs $M_{\text{recoil}}(\gamma)$ distribution for $\Upsilon(5S) \rightarrow \Upsilon(1S)\pi^+\pi^-$ events with ISR (after reweighting). The signal region is outlined in magenta.

Decay Process	Decay Model used in Mote Carlo Simulation
$\Upsilon(5S) \rightarrow \Upsilon(1S)\pi^+\pi^-$	PHSP
$\Upsilon(1S) \rightarrow \mu^+\mu^-$	PHSP
Initial state radiation	VectorISR
Final state radiation	PHOTOS

Table 7: Decay models used in Mote Carlo simulation of $\Upsilon(5S) \rightarrow \Upsilon(1S)\pi^+\pi^-$ with ISR.

374 backgrounds in the signal region.

375 To determine if we can use this MC sample to estimate the number of background events
 376 in the signal region, we divide the grand sideband region shown in Fig. 17 into four smaller
 377 regions as defined in Table 8 and observe if the number of events in MC scales uniformly
 378 to data across all regions. Table 9 shows the number of ISR MC events and data events
 379 within the regions of interest. We see that ISR MC does not scale uniformly across all
 380 regions. While ISR studies improve the quality of our analysis and provide us with useful
 381 information about the shape of this background in the signal region, including ISR into our
 382 analysis does not sufficiently improve the scaling between data and MC in different regions

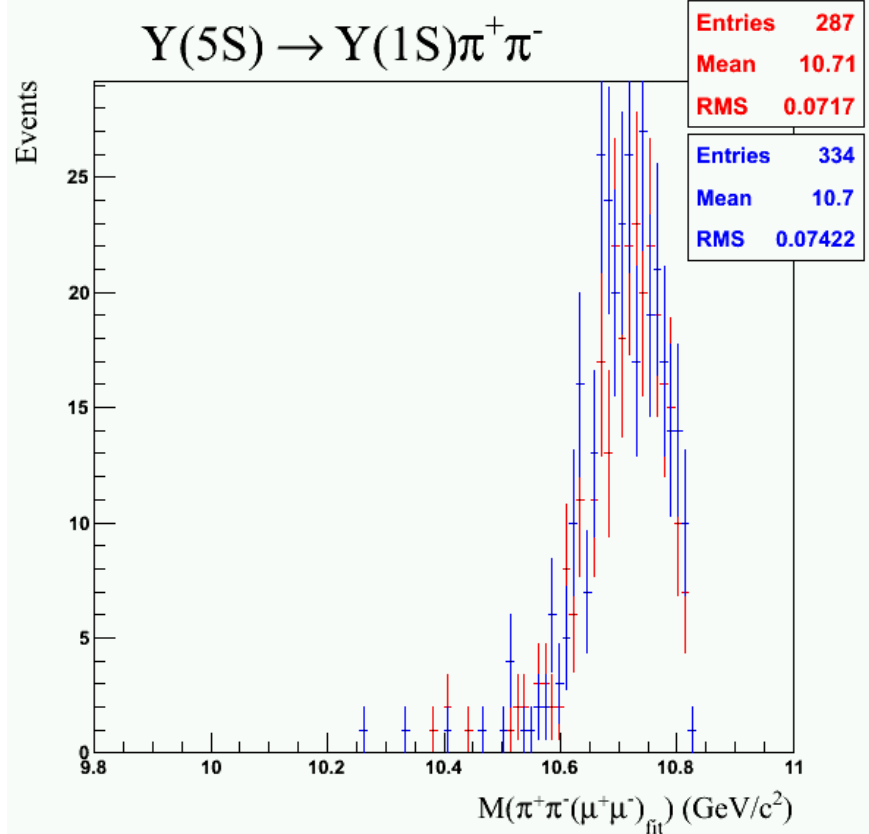


Figure 14: The distribution shown in blue is for events where $\Upsilon(5S) \rightarrow \Upsilon(1S)\pi^+\pi^-$ is generated using VVPIPI model [18] and $\Upsilon(1S) \rightarrow \mu^+\mu^-$ using VLL model [18]. The distribution shown in red is for events generated using PHSP model [18] for both processes. Neither samples contain ISR nor FSR, so they only differ by their decay models. The shapes of their $M(\pi^+\pi^-(\mu^+\mu^-)_{\text{fit}})$ distributions are very similar. Note that although there is a difference in efficiency between the two samples, this is unimportant for our analysis, because we are only interested in possible difference between the shapes of these distributions.

383 of grand sideband.

384 7 Contribution from $\Upsilon(5S) \rightarrow Z_b^{(\prime)\pm}\pi^\mp$

385 Belle previously reported [15] that charged Z_b and Z_b' states comprise, respectively, approx-
 386 imately 2.54% and 1.04% of the 1819 $\Upsilon(1S)\pi^+\pi^-$ (followed by $\Upsilon(1S) \rightarrow \mu^+\mu^-$) events
 387 observed with the full data sample. The overall reconstruction efficiency in Z_b analysis was
 388 estimated to be around 46%. This allows us to estimate that, with an ideal, *i.e.* 100%
 389 efficient detector, we would expect to detect, approximately, 100 Z_b and 41 Z_b' events.

390 To estimate cross-feed between Z_b and W_{bj} analyses, we generated approximately 50,000
 391 events for $\Upsilon(5S) \rightarrow Z_b^\pm\pi^\mp$ followed by $Z_b^\pm \rightarrow \Upsilon(1S)\pi^\mp$, $\Upsilon(1S) \rightarrow \mu^+\mu^-$. We also generated
 392 an additional 50,000 events for $\Upsilon(5S) \rightarrow Z_b^{\prime\pm}\pi^\mp$. These samples are 500 and 1000 larger
 393 than the numbers of such events which would be observed in data with an ideal detector.

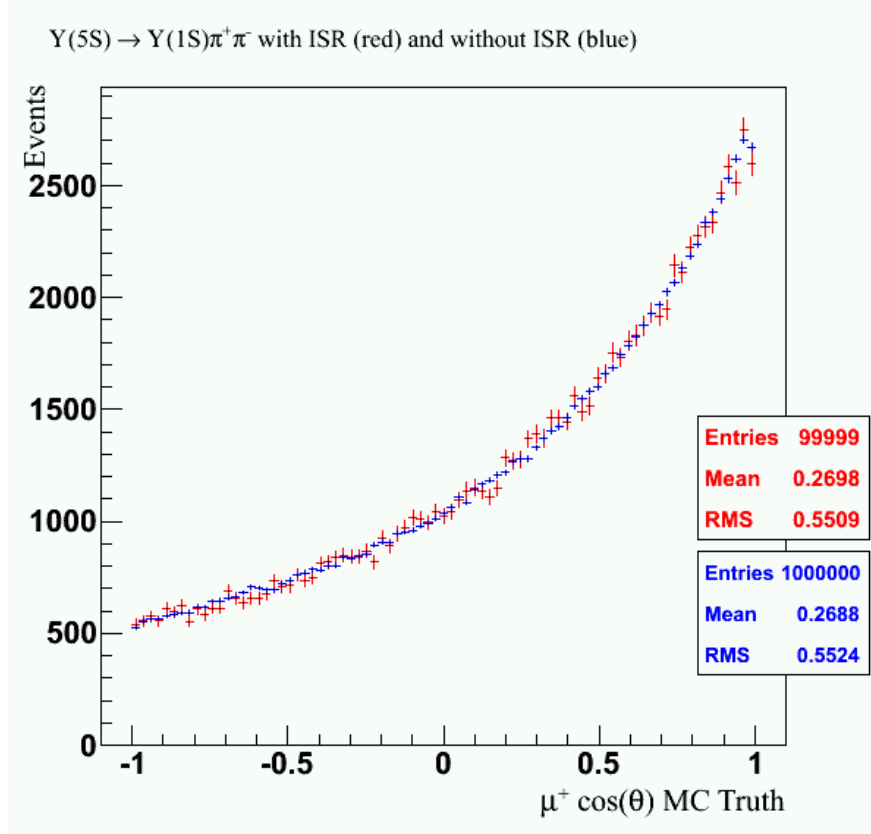


Figure 15: Distributions of $\cos \theta$ for μ^+ for $\Upsilon(5S) \rightarrow \Upsilon(1S)\pi^+\pi^-$ events. The distribution shown in red is for events generated with ISR while the distribution shown in blue is for events generated without ISR. Events in both distributions are generated using PHSP model for both $\Upsilon(5S) \rightarrow \Upsilon(1S)\pi^+\pi^-$ and $\Upsilon(1S) \rightarrow \mu^+\mu^-$. The blue distribution is normalized to the number of events in the red distribution.

Region Name	Boundary Definitions
Region 1	$10.72 \text{ GeV}/c^2 < M(\pi^+\pi^-(\mu^+\mu^-)_{\text{fit}}) < 10.80 \text{ GeV}/c^2$ $-0.2 \text{ GeV} < \Delta E < 0.2 \text{ GeV}$
Region 2	$10.49 \text{ GeV}/c^2 < M(\pi^+\pi^-(\mu^+\mu^-)_{\text{fit}}) < 10.72 \text{ GeV}/c^2$ $0.03 \text{ GeV} < \Delta E < 0.2 \text{ GeV}$
Region 3	$10.38 \text{ GeV}/c^2 < M(\pi^+\pi^-(\mu^+\mu^-)_{\text{fit}}) < 10.49 \text{ GeV}/c^2$ $-0.2 \text{ GeV} < \Delta E < 0.2 \text{ GeV}$
Excluded Region	$10.49 \text{ GeV}/c^2 < M(\pi^+\pi^-(\mu^+\mu^-)_{\text{fit}}) < 10.72 \text{ GeV}/c^2$ $-0.2 \text{ GeV} < \Delta E < 0.03 \text{ GeV}$

Table 8: Definitions of subdivisions of the grand sideband region. The Excluded Region is not considered in this analysis.

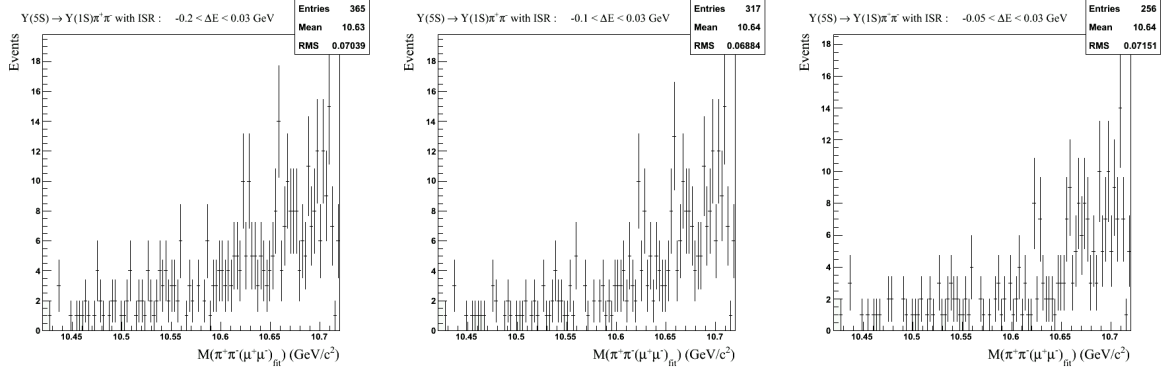


Figure 16: Distributions of $M(\pi^+\pi^-(\mu^+\mu^-)_{\text{fit}})$ for $\Upsilon(5S) \rightarrow \Upsilon(1S)\pi^+\pi^-$ with ISR in the signal region for different ΔE requirements. The leftmost distribution requires $-0.2 \text{ GeV} < \Delta E < 0.03 \text{ GeV}$, the middle distribution requires $-0.1 \text{ GeV} < \Delta E < 0.03 \text{ GeV}$, and the rightmost distribution requires $-0.05 \text{ GeV} < \Delta E < 0.03 \text{ GeV}$. The upper bound of ΔE is kept at 0.03 GeV for all distributions, since very few signal events fall beyond $\Delta E > 0.03 \text{ GeV}$.

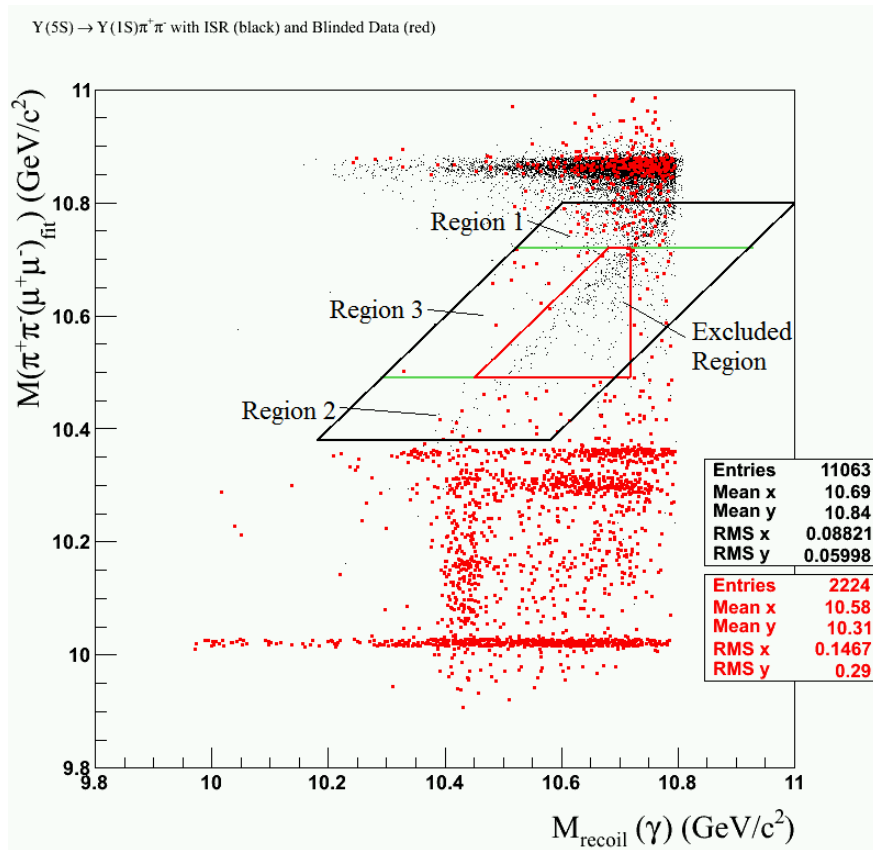


Figure 17: Subdivisions of the grand sideband region. The Excluded Region is not considered in this analysis.

Region	Number of events in ISR MC (N_{mc})	Number of events in blinded data (N_{data})	N_{mc}/N_{data}
Region 1	572	55	10.4
Region 2	28	23	1.2
Region 3	35	14	2.5

Table 9: Comparing the number of events in ISR MC and blinded data in the subdivided grand sideband Region

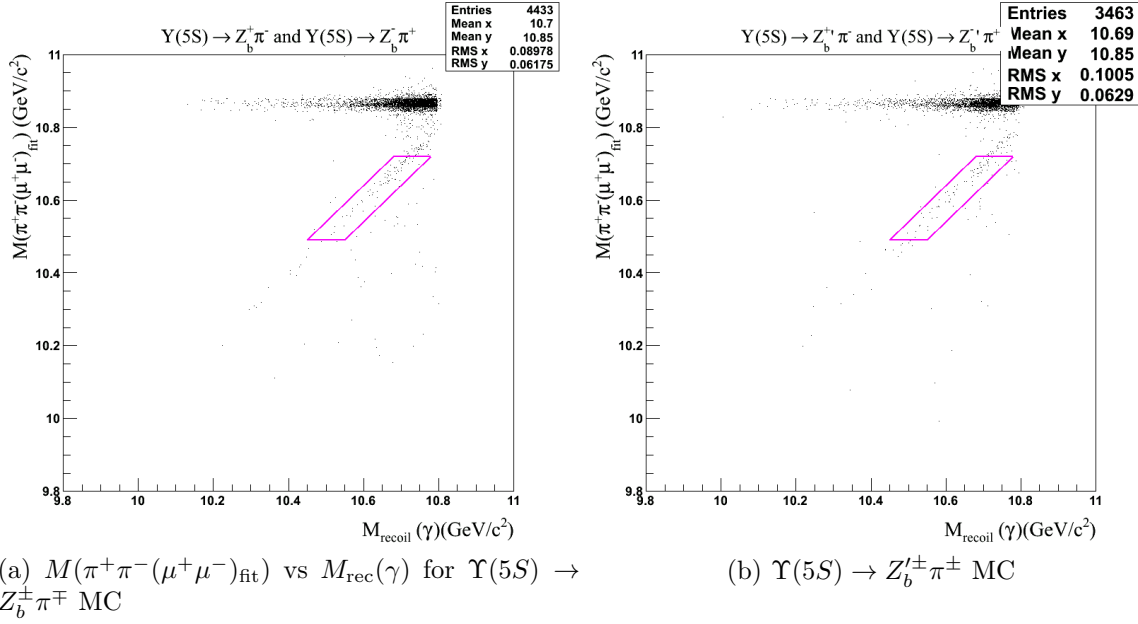
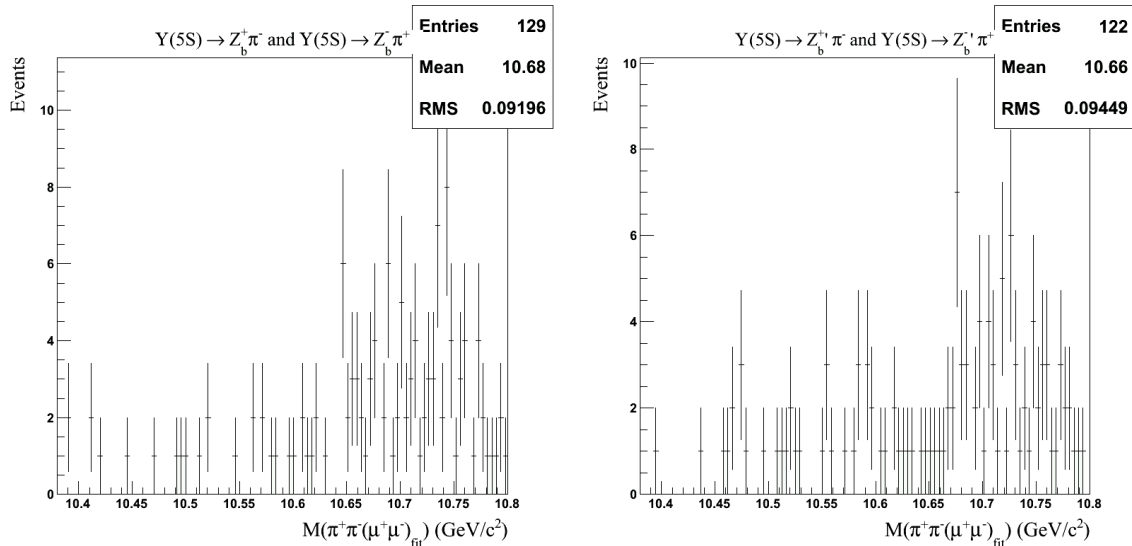


Figure 18: The distribution of $M(\pi^+\pi^-(\mu^+\mu^-)_{\text{fit}})$ vs $M_{\text{rec}}(\gamma)$ for $\Upsilon(5S) \rightarrow Z_b^{(\prime)\pm}\pi^{\mp}$ MC.

394 The distribution of $M(\pi^+\pi^-(\mu^+\mu^-)_{\text{fit}})$ vs $M_{\text{rec}}(\gamma)$ is shown in Fig. 18 for both samples
395 after applying our selection criteria for the W_{bj} analysis. Fig. 19 shows the distribution of
396 $M(\pi^+\pi^-(\mu^+\mu^-)_{\text{fit}})$ for events inside the signal and sideband region. It is important to note
397 that, approximately, only 2% of events fall in the signal region for each of the two samples.
398 Therefore, we expect less than 100 events from each of the two Z_b samples to be found in
399 the signal region for the W_{bj} analysis. As explained earlier in this section, to predict the
400 “contamination” of our signal region by Z_b events, this number has to be scaled down by
401 the factors of 500 and 1000 for contributions from Z_b and Z_b' , respectively. Therefore the
402 process $\Upsilon(5S) \rightarrow Z_b^{(\prime)\pm}\pi^{\mp}$ in total, has negligible cross-feed contribution in the signal region
403 and can be safely ignored.



(a) $M(\pi^+\pi^-(\mu^+\mu^-)_{\text{fit}})$ for $\Upsilon(5S) \rightarrow Z_b^\pm \pi^\mp$ MC. (b) $M(\pi^+\pi^-(\mu^+\mu^-)_{\text{fit}})$ for $\Upsilon(5S) \rightarrow Z_b'^\pm \pi^\mp$ MC.

Figure 19: The distribution of $M(\pi^+\pi^-(\mu^+\mu^-)_{\text{fit}})$ for $\Upsilon(5S) \rightarrow Z_b^{(\prime)\pm} \pi^\mp$ MC for events inside the signal and sideband region.

8 Fitting

8.1 Signal and Background PDFs

To extract signal yield, we perform a one-dimensional extended unbinned ML fit to the variable $M(\pi^+\pi^-(\mu^+\mu^-)_{\text{fit}})$ using RooFit [22]. We model the signal distribution of $M(\pi^+\pi^-(\mu^+\mu^-)_{\text{fit}})$ as a Breit-Wigner convolved with the sum of two Gaussians (to simulate effects of detector resolution as shown in Fig. 5). The observed width and shape of $M(\pi^+\pi^-(\mu^+\mu^-)_{\text{fit}})$ distribution in signal MC remains practically the same after applying our ΔE requirement and after including ISR. Therefore, we fix the width of our signal PDF. We set the width of the Breit-Wigner to be $\sigma_{BW} = 15 \text{ MeV}/c^2$ to match the intrinsic width of Z_b and Z_b' . The widths of the Gaussians used in convolution are $\sigma_{G_1} \approx 3 \text{ MeV}/c^2$ and $\sigma_{G_2} \approx 7.7 \text{ MeV}/c^2$ to match the widths obtained from the fit to $M(\pi^+\pi^-(\mu^+\mu^-)_{\text{fit}})$ resolution. We let mean of Breit-Wigner float within the fit, as W_{bJ} could be observed at different invariant masses for different spins J . Table 10 lists the values of parameters used in our signal PDF model.

We use an exponential $e^{\lambda x}$ to model background contributions due to ISR as well as possible non-resonant contribution from dimuon continuum events. Strictly speaking, the background distribution deviates from an exponential at $M(\pi^+\pi^-(\mu^+\mu^-)_{\text{fit}}) \approx 10.75 \text{ GeV}/c^2$ because of the phase boundary at $M_{\text{rec}}(\gamma) \approx 10.75 \text{ GeV}/c^2$ seen in Fig. 4. This ever-present effect can be seen in figures showing the distribution of $M(\pi^+\pi^-(\mu^+\mu^-)_{\text{fit}})$ for background events with our ΔE requirement (*e.g.* see Fig. 14, Fig. 20b, Fig. 20c). This shortcoming of our analysis will be taken care of in the next version of this Note. We would like to remark that the observed fall-off effect is easy to understand and describe in the model used for fitting, as it is exclusively due to the boundary of phase space.

To estimate the number of background events we expect in the signal region, we per-

Quantity	Value Used in Signal PDF (MeV/c ²)
σ_{BW}	15
Mean of BW	floats between 10.38 and 10.80 GeV/c ²
σ_{G_1}	3.0 ± 0.1
σ_{G_2}	7.7 ± 0.2
Fraction of Gaussian 1	0.73 ± 0.01
Fraction of Gaussian 2	0.27 ± 0.01
Mean of both Gaussians	$(-3.8 \pm 0.2) \cdot 10^{-4}$

Table 10: Values of fixed quantities in the signal PDF model.

427 form an extended unbinned maximum likelihood fit to data only in the sideband regions.
428 To account for uncertainty in the number of data events in the sideband region, we fit
429 $M(\pi^+\pi^-(\mu^+\mu^-)_{\text{fit}})$ within the range of 10.38 GeV/c² and 10.80 GeV/c² when extracting
430 signal yield. This range corresponds to the signal region and sideband regions combined.
431 From the fit, we obtain $\lambda = 3.7951$. We extract 59 ± 11 background events in the signal
432 region and sideband regions combined. We expect 27 ± 5 of these background events to be
433 in the signal region alone. Fits to W_{b0} signal MC, $\Upsilon(5S) \rightarrow \Upsilon(1S)\pi^+\pi^-$ MC with ISR MC,
434 and data in the sidebands are shown in Fig. 20.

435 8.2 Confidence Belts

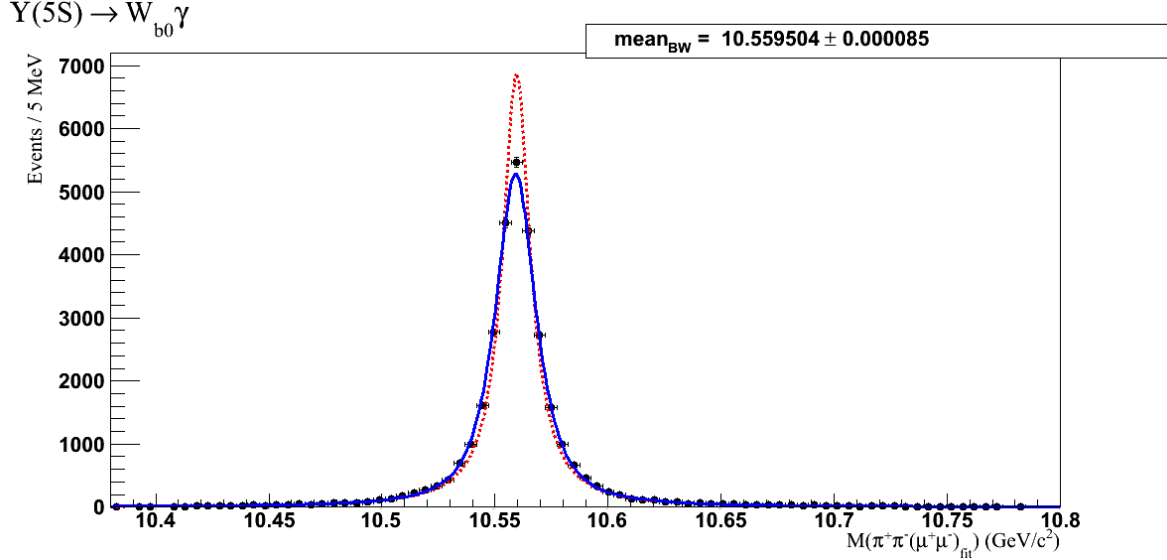
436 To construct a 90% confidence belt, we perform ensemble tests. Each ensemble test consists
437 of 1000 toy MC experiments. In each toy MC experiment, we generate N_{sig} signal events
438 and N_{bkg} background events according to their respective PDF lineshapes used for fitting
439 signal and background. We then fit the generated events in the range $10.38 \text{ GeV}/c^2 <$
440 $M(\pi^+\pi^-(\mu^+\mu^-)_{\text{fit}}) < 10.80 \text{ GeV}/c^2$ to our combined signal and background PDF to extract
441 the fitted number of signal events $N_{\text{sig}}^{\text{fit}}$.

442 We construct our 90% confidence belt by performing ensemble tests with $N_{\text{bkg}}^{\text{gen}} = 59$ for
443 values of $N_{\text{sig}}^{\text{gen}}$ from 0 to 70. We additionally construct a 90% confidence belt where we allow
444 Poisson fluctuation in $N_{\text{bkg}}^{\text{gen}}$. These confidence belts are shown in Fig. 21.

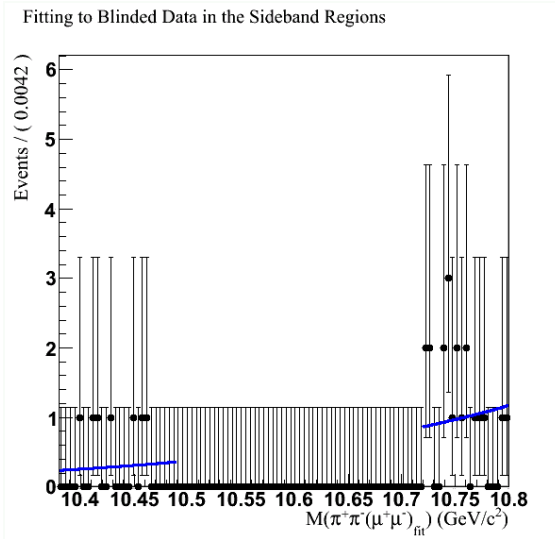
445 8.3 Linearity Study

446 To validate our fitting procedures, we perform a linearity study using ensemble tests. En-
447 semble tests are generated as described in Section 8.2. For each ensemble test of 1000 toy
448 MC experiments, we calculate the average number of signal events from the fit and the error
449 associated with the average. We vary $N_{\text{sig}}^{\text{gen}}$ from 0 to 10 in steps of 1 and from 10 to 50 in
450 steps of 5 while fixing $N_{\text{bkg}} = 59$.

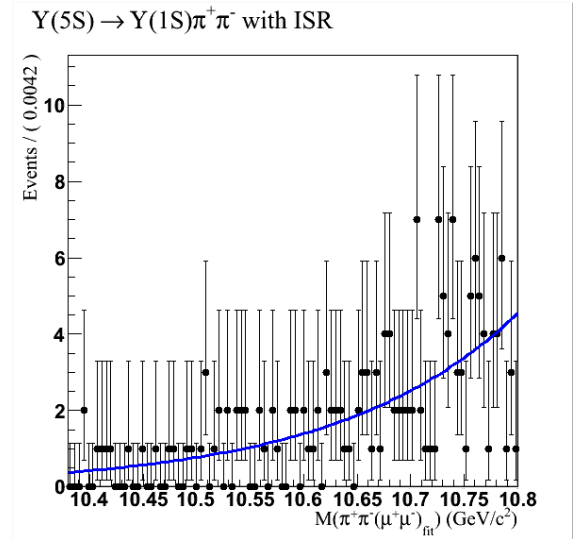
451 We plot the average number of signal events from the fit against $N_{\text{sig}}^{\text{gen}}$ as shown in
452 Fig. 22. Fig. 23 displays distributions of $N_{\text{sig}}^{\text{fit}}$ for certain values of $N_{\text{sig}}^{\text{gen}}$. When $N_{\text{sig}}^{\text{gen}}$ is large,
453 the distribution of $N_{\text{sig}}^{\text{fit}}$ is unbiased. For small $N_{\text{sig}}^{\text{gen}}$, however, we see an asymmetry in the



(a) Fit result for the distribution of $M(\pi^+\pi^-(\mu^+\mu^-)_{\text{fit}})$ for signal MC in the signal and sideband region. The Breit-Wigner shape is shown in red. The blue distribution is the Breit-Wigner convolved with the sum of two Gaussians.



(b) Fit result for the distribution of $M(\pi^+\pi^-(\mu^+\mu^-)_{\text{fit}})$ for data in the sideband region.



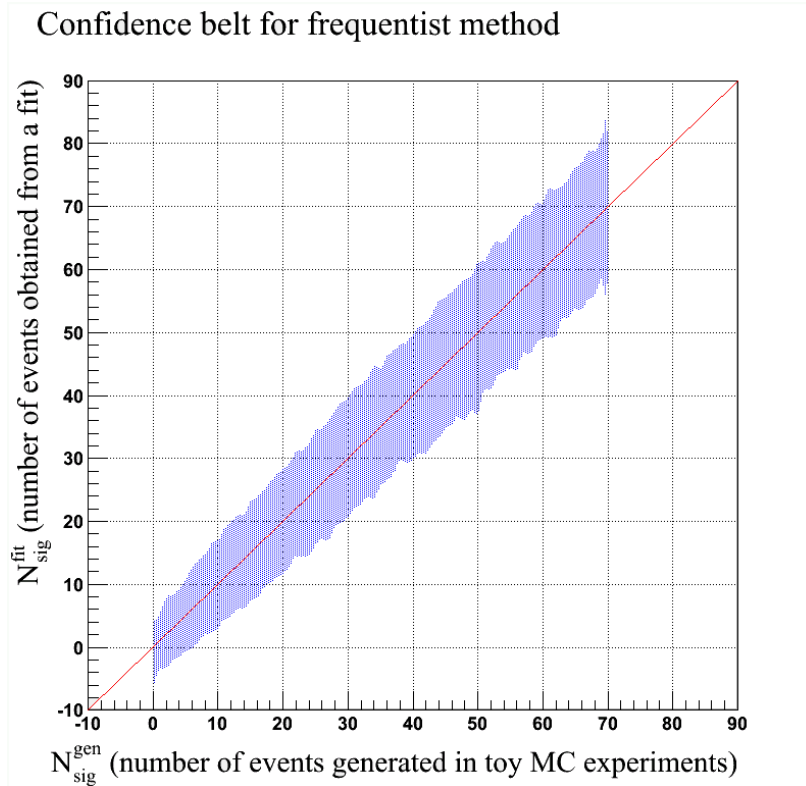
(c) Fit result for the distribution of $M(\pi^+\pi^-(\mu^+\mu^-)_{\text{fit}})$ for $\Upsilon(5S) \rightarrow \Upsilon(1S)\pi^+\pi^-$ with ISR for events in the signal region.

Figure 20: Fitting background MC and data

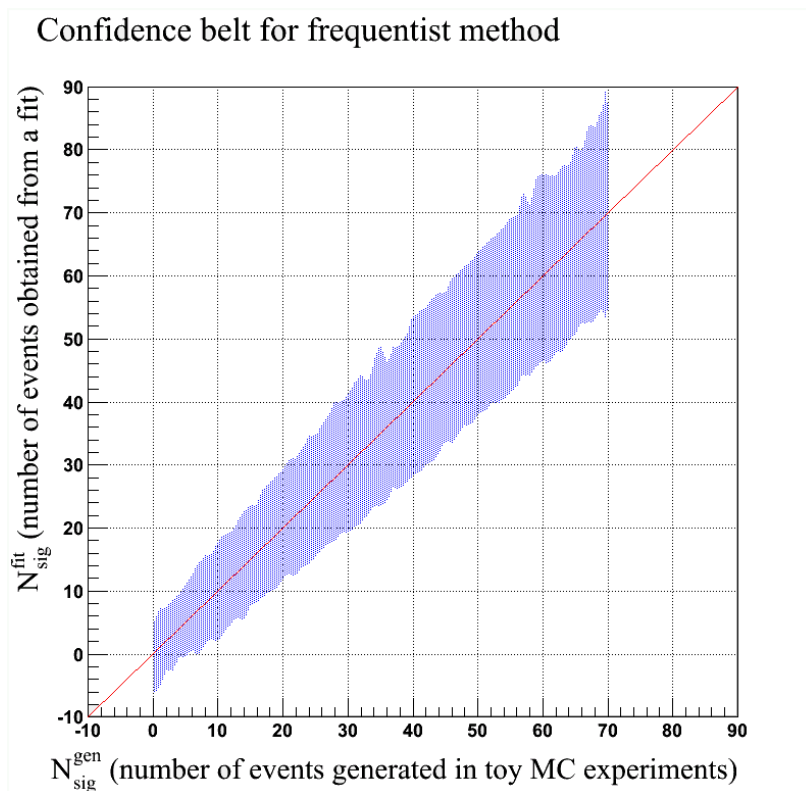
454 distribution of $N_{\text{sig}}^{\text{fit}}$, indicating some bias. This effect is often observed for small statistics
 455 and is not unexpected.

456 8.4 Sensitivity Estimation

457 We estimate the upper limit on the branching fraction and visible cross section of $\Upsilon(5S) \rightarrow$
 458 γW_{bJ} in the absence of signal by performing an extended unbinned maximum likelihood fit



(a) Does not include Poisson fluctuations in $N_{\text{bkg}}^{\text{gen}}$



(b) Includes Poisson fluctuations in $N_{\text{bkg}}^{\text{gen}}$.

Figure 21: 90% confidence belts for frequentist method.

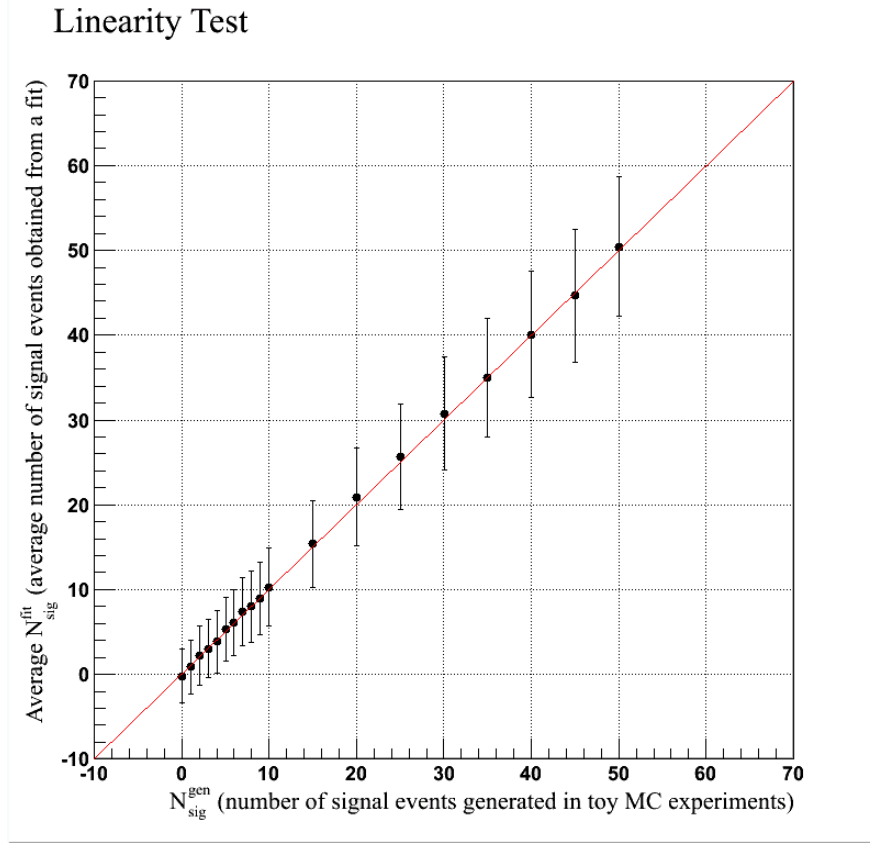


Figure 22: Average $N_{\text{sig}}^{\text{fit}}$ for varying values of $N_{\text{sig}}^{\text{gen}}$.

459 on toy MC generated according to the fit to the data sidebands. We generate 1000 toy MC
 460 samples with 59 background events, fit our combined signal and background shape to each
 461 sample, and then average the resulting signal yields. There is an average signal yield of
 462 -0.2 ± 3.2 events. Note that in Fig. 22, this average signal yield corresponds to the value
 463 plotted at $N_{\text{sig}}^{\text{gen}} = 0$. Using the confidence belt in Fig. 21, we determine the 95% confidence
 464 level upper limit on the number of signal events to be 10 events. We calculate the upper
 465 limit on the branching fraction in the absence of signal as follows:

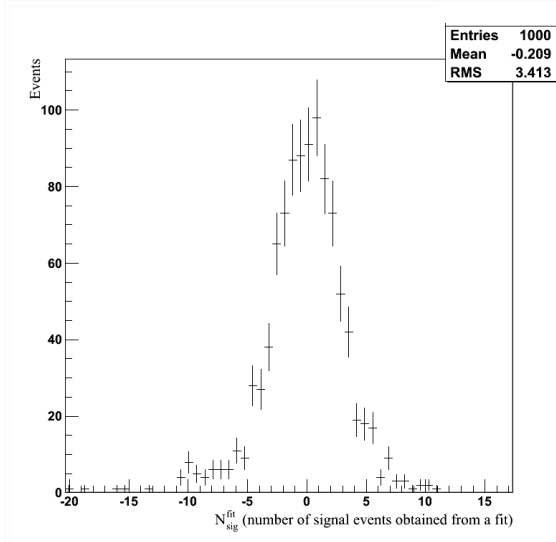
$$\mathcal{B}(\Upsilon(5S) \rightarrow \gamma W_{bJ}) \cdot \mathcal{B}(W_{bJ} \rightarrow \Upsilon(1S)\rho^0) = \frac{N_{\text{sig}}}{\epsilon \cdot N_{\Upsilon(5S)} \cdot \mathcal{B}(\Upsilon(1S) \rightarrow \mu^+\mu^-) \cdot \mathcal{B}(\rho^0 \rightarrow \pi^+\pi^-)} \quad (4)$$

466 where $N_{\Upsilon(5S)}$ is the number of $\Upsilon(5S)$ and ϵ is our reconstruction efficiency. Using Eq. 4, we
 467 determine the upper limit on the branching fraction in the absence of signal to be 2.4×10^{-5} .

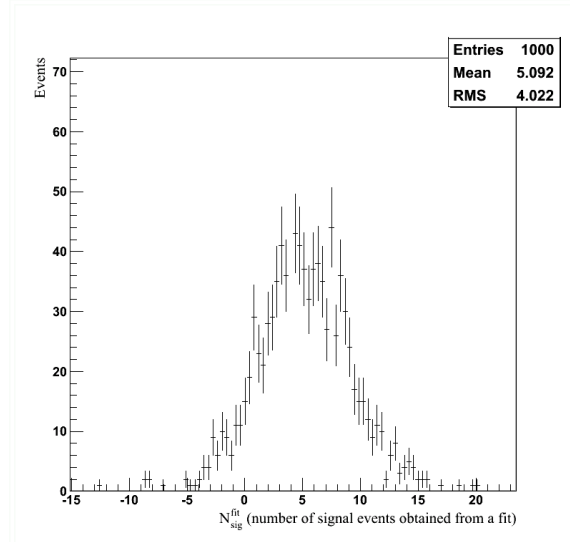
468 We calculate the visible cross section using

$$\sigma_{\text{vis}} = \frac{N_{\text{sig}}}{\epsilon \mathcal{B}(\Upsilon(1S) \rightarrow \mu^+\mu^-) \mathcal{B}(\rho^0 \rightarrow \pi^+\pi^-) \mathcal{L}} \quad (5)$$

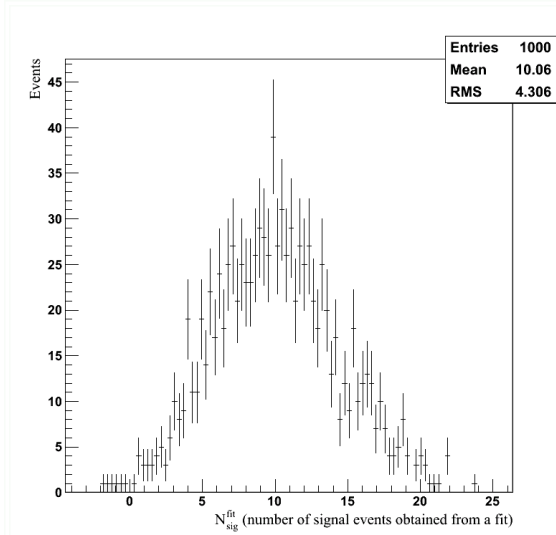
469 where \mathcal{L} is the integrated luminosity. We find $\sigma_{\text{vis}} = (0.115 \pm 0.006)$ fb. All values used to
 470 calculate the branching fraction and visible cross section are shown in Table 11.



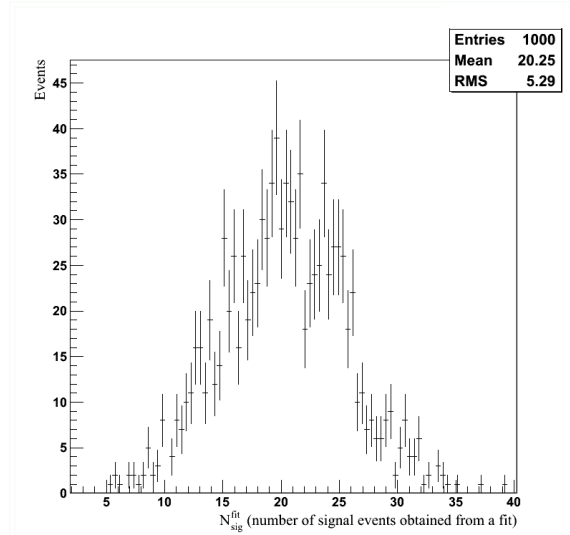
(a) Distribution of $N_{\text{sig}}^{\text{fit}}$ for an ensemble test with $N_{\text{sig}}^{\text{gen}} = 0$ and $N_{\text{bkg}}^{\text{gen}} = 59$.



(b) Distribution of $N_{\text{sig}}^{\text{fit}}$ for an ensemble test with $N_{\text{sig}}^{\text{gen}} = 5$ and $N_{\text{bkg}}^{\text{gen}} = 59$.



(c) Distribution of $N_{\text{sig}}^{\text{fit}}$ for an ensemble test with $N_{\text{sig}}^{\text{gen}} = 10$ and $N_{\text{bkg}}^{\text{gen}} = 59$.



(d) Distribution of $N_{\text{sig}}^{\text{fit}}$ for an ensemble test with $N_{\text{sig}}^{\text{gen}} = 20$ and $N_{\text{bkg}}^{\text{gen}} = 59$.

Figure 23: $N_{\text{sig}}^{\text{fit}}$ Distributions for ensemble tests with different $N_{\text{sig}}^{\text{gen}}$.

471 9 Summary

472 In this analysis, we describe a search for a new molecular state W_{bJ} which could be pro-
 473 duced in the radiative transition $\Upsilon(5S) \rightarrow \gamma W_{bJ}$ followed by the decays $W_{bJ} \rightarrow \Upsilon(1S)\rho^0$,
 474 $\Upsilon(1S) \rightarrow \mu^+\mu^-$, $\rho^0 \rightarrow \pi^+\pi^-$. We fully reconstruct the signal final state consisting of two
 475 muons, two pions, and a photon. We perform a blind analysis by optimizing our selection
 476 criteria and analysis techniques using only MC samples before applying them to data. To
 477 search for the presence of W_{bJ} in Belle data, we propose to "unblind" 15% of the data in

Quantity	Value
N_{sig}	10
ϵ	$(29 \pm 0.17)\%$
$N_{\Upsilon(5S)}$	$(6.53 \pm 0.66) \cdot 10^6$
$\mathcal{B}(\Upsilon(1S) \rightarrow \mu^+ \mu^-)$	$(2.48 \pm 0.05)\%$
$\mathcal{B}(\rho^0 \rightarrow \pi^+ \pi^-)$	99.8%
\mathcal{L}	121.4 fb^{-1}

Table 11: Values of quantities used to calculate upper limits on visible cross section and the branching fraction. Uncertainty in $\mathcal{B}(\rho^0 \rightarrow \pi^+ \pi^-)$ is negligible. Note that, for purposes of estimating upper limits, we use $N_{\text{sig}} = 10$, which is the 95% CL boundary of the 90% CL frequentist belt shown in Fig. 21 for $N_{\text{sig}}^{\text{fit}} = 3$, according to the result of the fit $N_{\text{sig}}^{\text{fit}} = -0.2 \pm 3.2$.

478 the signal region and then fit a one-dimensional distribution of $M(\pi^+ \pi^- (\mu^+ \mu^-)_{\text{fit}})$ using the
479 aforementioned models for signal and background shapes. We will use our confidence belt
480 (Fig. 21) to either claim a discovery of W_{bJ} or establish an upper limit on the signal produc-
481 tion rate (branching fraction) for the radiative decay $\Upsilon(5S) \rightarrow \gamma W_{bJ}$. The following sources
482 of systematic uncertainties will be considered in our final estimate of the upper limit of the
483 branching fraction of $\Upsilon(5S) \rightarrow \gamma W_{bJ}$:

- 484 • Number of $\Upsilon(5S)$
- 485 • Signal Reconstruction Efficiency
- 486 • Daughter Branching Fractions
- 487 • MC statistics
- 488 • PDF parameterization
- 489 • Fit bias
- 490 • Trigger efficiency

491 10 Appendix

492 10.1 Final State Radiation

493 In the version of package PHOTOS used by Belle, the minimum FSR photon energy (eval-
494 uated in the center of mass frame of charged particle's parent) is calculated as follows:

$$E(\gamma_{FSR}) = (\text{XPHCUT}) \cdot 0.5 \cdot M(\text{parent}) \quad (6)$$

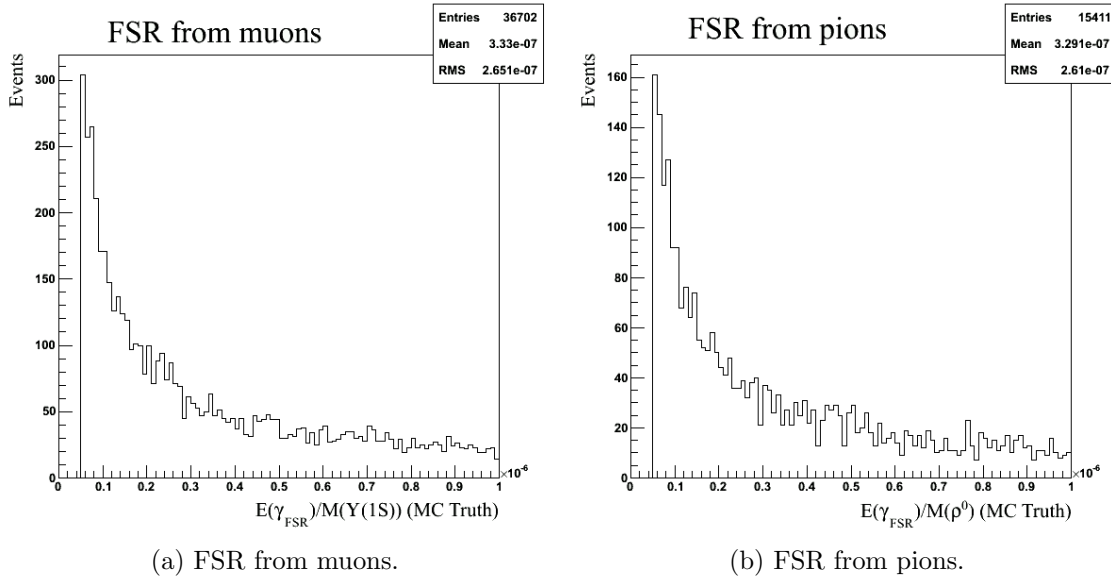


Figure 24: Final state radiation from charged tracks

495 where XPHCUT is a hardcoded constant set to 0.01. Hence, the minimum FSR energy is
 496 approximately 4 MeV for pions ($M(\rho^0) = 770$ MeV) and 50 MeV for muons ($M(\Upsilon(1S)) =$
 497 9.46 GeV). The lower limit on FSR energy for muons is too high, so we lowered the
 498 value of XPHCUT to 10^{-7} . To accomplish this, we changed XPHCUT=0.01D0 to XPH-
 499 CUT=0.0000001D0, recompiled the phocin.F source code and then rebuilt EvtGen with an
 500 updated PHOTOS library.

501 To verify that XPHCUT was successfully lowered to 10^{-7} , we plot the ratios $\frac{E(\gamma_{FSR})}{M(\Upsilon(1S))}$
 502 and $\frac{E(\gamma_{FSR}^\rho)}{M(\rho)}$ as generated in Fig. 24. Because these quantities are bounded from below by
 503 $XPHCUT \cdot 0.5$, we prove that XPHCUT was successfully lowered.

504 References

- 505 [1] A. Bondar et al. Observation of two charged bottomonium-like resonances in $Y(5S)$
 506 decays. *Phys. Rev. Lett.*, 108:122001, 2012.
- 507 [2] I. Adachi et al. Evidence for a $Z_b^0(10610)$ in Dalitz analysis of $\Upsilon(5S) \rightarrow Y(nS)\pi^0\pi^0$.
 508 2012.
- 509 [3] P. Krokovny et al. First observation of the $Z_b^0(10610)$ in a Dalitz analysis of $\Upsilon(10860)$
 510 $\rightarrow \Upsilon(nS)\pi^0\pi^0$. *Phys. Rev.*, D88(5):052016, 2013.
- 511 [4] A. Garmash et al. Observation of $Z_b(10610)$ and $Z_b(10650)$ Decaying to B Mesons.
 512 *Phys. Rev. Lett.*, 116(21):212001, 2016.
- 513 [5] L. M. Lederman. The discovery of the Upsilon, bottom quark, and B mesons. In
 514 *The Rise of the standard model: Particle physics in the 1960s and 1970s. Proceedings,*
 515 *Conference, Stanford, USA, June 24-27, 1992*, pages 101–113, 1992.

- 516 [6] M. Tanabashi et al. Review of Particle Physics. *Phys. Rev.*, D98(3):030001, 2018.
- 517 [7] S. Godfrey and N. Isgur. Mesons in a Relativized Quark Model with Chromodynamics.
518 *Phys. Rev.*, D32:189–231, 1985.
- 519 [8] S. Godfrey and K. Moats. Bottomonium Mesons and Strategies for their Observation.
520 *Phys. Rev.*, D92(5):054034, 2015.
- 521 [9] S. Godfrey, K. Moats, and E. S. Swanson. B and B_s Meson Spectroscopy. *Phys. Rev.*,
522 D94(5):054025, 2016.
- 523 [10] A. E. Bondar, R. V. Mizuk, and M. B. Voloshin. Bottomonium-like states: Physics case
524 for energy scan above the $B\bar{B}$ threshold at Belle-II. *Mod. Phys. Lett.*, A32(04):1750025,
525 2017.
- 526 [11] A. E. Bondar, A. Garmash, A. I. Milstein, R. Mizuk, and M. B. Voloshin. Heavy quark
527 spin structure in Z_b resonances. *Phys. Rev.*, D84:054010, 2011.
- 528 [12] Stephen Lars Olsen. A New Hadron Spectroscopy. *Front. Phys.(Beijing)*, 10(2):121–154,
529 2015.
- 530 [13] M. B. Voloshin. Radiative transitions from Upsilon(5S) to molecular bottomonium.
531 *Phys. Rev.*, D84:031502, 2011.
- 532 [14] W. Altmannshofer et al. The Belle II Physics Book, arXiv:hep-ex/1808.10567, 2018.
- 533 [15] I. Adachi et al. Study of Three-Body $Y(10860)$ Decays, arXiv:hep-ex/1209.6450,
534 BELLE-CONF-1272, 2012.
- 535 [16] D. J. Lange. The EvtGen particle decay simulation package. *Nucl. Instrum. Meth.*,
536 A462:152–155, 2001.
- 537 [17] S. Agostinelli et al. GEANT4: A Simulation toolkit. *Nucl. Instrum. Meth.*, A506:250–
538 303, 2003.
- 539 [18] A. Ryd, D. Lange, N. Kuznetsova, S. Versille, M. Rotondo, D. P. Kirkby, F. K. Wuerth-
540 wein, and A. Ishikawa. EvtGen: A Monte Carlo Generator for B -Physics. 2005.
- 541 [19] E. Barberio and Z. Was. PHOTOS: A Universal Monte Carlo for QED radiative cor-
542 rections. Version 2.0. *Comput. Phys. Commun.*, 79:291–308, 1994.
- 543 [20] J. Brodzicka et al. Physics Achievements from the Belle Experiment. *PTEP*,
544 2012:04D001, 2012.
- 545 [21] M. Benayoun, S. I. Eidelman, V. N. Ivanchenko, and Z. K. Silagadze. Spectroscopy at B
546 factories using hard photon emission. *Mod. Phys. Lett.*, A14:2605–2614, 1999. [Frascati
547 Phys. Ser.15(1999)].
- 548 [22] Wouter Verkerke and David P. Kirkby. The RooFit toolkit for data modeling. *eConf*,
549 C0303241:MOLT007, 2003. [186(2003)].